

Milky Way total Mass derived by Rotation Curve and Globular Cluster kinematics from Gaia EDR3

Jianling Wang^{1*}, Francois Hammer², Yanbin Yang²

¹ CAS Key Laboratory of Optical Astronomy, National Astronomical Observatories, Beijing 100101, China,

² GEPI, Observatoire de Paris, CNRS, Place Jules Janssen 92195, Meudon, France.

Received ; accepted

ABSTRACT

Using action-based distribution function for the dynamical model of the Milky Way we have estimated its total mass and its density profile. Constraints are coming from the globular cluster proper motions from Gaia EDR3, from the rotation curve based on Gaia DR2 data, and from the vertical force data. We use Bayesian Markov chain Monte Carlo method to explore the parameters, for which the globular cluster distribution function and the Galactic potential are fully constrained. Numerical simulations are used to study the uncertainties on the potential constraint if considering a possible massive Large Magellanic Cloud (LMC). We found that a massive LMC ($1.5 \times 10^{11} M_{\odot}$) will affect the MW mass measurement at large radius, which includes both the Milky Way and the LMC. We also use the FIRE2 Latte cosmological hydrodynamic simulations to make mock data set from a Milky-Way like galaxy that includes many unrelaxed substructures. We test the effect of these unrelaxed substructures on the final results, and found that the measured rotation curve fluctuated around input value within 5 percent. By keeping a large freedom in choosing a priori mass profile for both baryonic and dark matter leads a total mass of the MW that ranges from $5.36^{+0.81}_{-0.68} \times 10^{11} M_{\odot}$ to $7.84^{+3.08}_{-1.97} \times 10^{11} M_{\odot}$. This includes the contribution of a putative massive LMC and significantly narrows the MW total mass range published earlier. Such total mass leads to dark matter density at solar position of $0.34^{+0.02}_{-0.02} \text{ GeV cm}^{-3}$.

Key words: globular clusters: general – Galaxy: halo – Galaxy: kinematics and dynamics – Galaxy: structure

1 INTRODUCTION

The Galactic Dark Matter (DM) mass density profile and total mass are of the most importance in modern astrophysics and cosmology. The Milky Way (MW) provides an unique opportunity for testing cosmology at small scales and the galaxy formation process. The mass density profile and the total mass of the MW governs its number of sub-halos of MW mass galaxies, which is intimately related to low mass scale discrepancies to standard cold dark matter model (Λ CDM). For example, the missing satellite and the too-big-to-fail problems (Moore et al. 1999; Boylan-Kolchin, Bullock & Kaplinghat 2011; Wang et al. 2012; Cautun et al. 2014) are all closely related to the total mass of MW. Therefore, the accurate measurement of the total mass of MW is also important for understanding dwarf dynamics and their accretion history, and also tests cosmological predictions. Gaia (DR2 and even more EDR3) data become sufficiently precise to constraint the orbital properties of MW dwarfs. It can be used to fur-

ther test whether the MW and its cortege of dwarfs are similar to Λ CDM halo and sub-haloes (Riley et al. 2019; Hammer et al. 2020; Li et al. 2021), which again depends on the MW total mass.

The elusive DM emits no light and can be only detected using indirect methods. Since DM affects dynamics, the kinematics of various luminous tracers have been investigated to derive its mass and density profile. In the inner region, the disk rotation curve (RC) is usually measured with tracers having circular motions, for instance, classic Cepheids (Mróz et al. 2019), open clusters, HII region (Sofue 2012). In the halo region, the DM mass density profile is usually derived from kinematic analysis from halo tracers, for examples, dwarfs assumed to be long-lived satellites (Callingham et al. 2019), globular clusters (Eadie & Jurić 2019; Vasiliev 2019b; Watkins et al. 2019), stellar streams (Küpper et al. 2015; Gibbons, Belokurov & Evans 2014; Bowden, Belokurov & Evans 2015; Malhan & Ibata 2019), and halo stars (Kafle et al. 2012, 2014). A comprehensive review on the methods of total Galactic mass measurement can be found in Wang et al. (2020). Even though the total mass of MW have been

* E-mail: wjianl@bao.ac.cn

measured for a few decades, its actual value is still uncertain by a large factor (see Figure 1 of Wang et al. 2020).

The *Gaia* satellite has revolutionized the Galactic mass determination by providing accurate proper motion for a far much larger number of stars than ever done before. By combining the large sky spectroscopic survey in the ground such as SDSS (York et al. 2000) and LAMOST (Cui et al. 2012; Zhao et al. 2012), accurate 6D phase-space coordinates can provide strong constraint on the Galactic DM profile and total mass. It is expected in the following years that the *Gaia* will continue to improve precision and accuracy of the astrometry and photometry for more and more stars (Gaia Collaboration et al. 2020).

Understanding how the MW is structured and its assembly history is now a central task in using those unprecedented data. Dynamical modeling is one of most important tool to understand how the MW is structured. Dynamical modeling with action-based distribution function DF ($f(\mathbf{J})$) has provided a major progress in this field. In an axisymmetric system, the action integrals \mathbf{J}_r , \mathbf{J}_z , \mathbf{J}_ϕ are the integral of motions, quantifying the amplitude of oscillations in the radius and in the vertical directions, and angular momentum around the symmetric axis, respectively (Vasiliev 2019a; Binney 2020). These actions are adiabatically invariants and conserved under slowly evolution of the potential, and in absence of energy exchanges. Consequently, $f(\mathbf{J})$ is invariant too. A system is fully determined as long as the DFs of each component are specified, and from these DFs any measurement can be predicted for the model (Binney 2020).

Recent progresses with large spectroscopic surveys and *Gaia* data reveal that the stellar halo is made of unrelaxed substructures and furthermore there might be a large scale velocity gradient induced by the passage of the Large Magellanic Cloud (LMC), if the latter is very massive. These two effects may affect the assumption of equilibrium and relaxed system in any dynamical modeling, which should be addressed when interpreting modeling results.

In this work, we use new released data of *Gaia* EDR3 to derive the proper motion of Galactic globular clusters. The improvement by about a factor of 2 in proper motion and the similar reduction of the systematic error (Gaia Collaboration et al. 2020) make the measurement on the MW DM density profile improvement much better than ever. Combining the new data with the accurate disk RC from *Gaia* DR2 (Eilers et al. 2019), we can model the Galactic globular clusters (GCs) with the action-based distribution function, and then constrain Galactic DM profile. By using N-body simulation one can test the bias introduced by a possible massive LMC. By using realistic cosmological hydrodynamic simulations from the FIRE2 suite, we can test the effects of unrelaxed substructures.

The paper is organized as it follows: Section 2 presents the measurement of GC proper motions and their uncertainties with *Gaia* EDR3. Section 3 describes the additional observation data used to constrain the rotation curve (RC) measurement. Section 4 presents the detail on the dynamical modeling with action-based DF method, and the results are shown in section 5. In section 6 we use numerical simulations to investigate the possible effect of a massive LMC passing by to the MW mass measurement, as well as the effects due to unrelaxed substructures. Lastly, we conclude our results in Section 7.

2 THE PROPER MOTION OF MW GCS

In this section we describe the method used to derive the mean proper motion and its associated uncertainties considering the systematic errors in the *Gaia* EDR3.

2.1 Determining the Mean Proper Motions of GCs with *Gaia* EDR3

We follow the procedure of Vasiliev (2019b) to derive the mean proper motion (PM) and its associated uncertainties for each cluster. We have used the publicly released code by Vasiliev (2019b). Here we briefly describe the method (more details in Vasiliev (2019b,c)).

The stars around each GC are clumped in PM space, which include member stars and field stars. For each cluster, a probabilistic Gaussian mixture model is applied to the PM distribution for stars and determine their membership probability. A spherical Plummer profile is assumed for the prior functional form of membership probability, for which the scale radius of Plummer profile is allowed to be adjusted during the fitting. An isotropic Gaussian function is assumed for the intrinsic PM dispersion for the cluster members. By adopting this spatially dependent prior for the membership probability, the intrinsic (error-deconvolved) parameters of the distributions of both member and non-member stars are derived. Since there is non-negligible spatially correlated systematic errors in the PM of *Gaia* data, this systematic error can be addressed by adopting the PM correlation function as below.

Lindgren et al. (2018) and Lindgren et al. (2021) have explored the angular covariances of proper motion based on the high precision quasar sample for both GAIA DR2 and EDR3 samples. They have found that the covariance of proper motion errors can be well fitted with an exponential function. This exponential function can fit well the covariance at large scales (upper panel of Figure 1), but it fails to capture the variation at small scales, well below 1 degree (bottom panel of Figure 1). Following Vasiliev (2019c), we modified the fitting function of Lindgren et al. (2021) by adding another exponential function to capture the small scale variation of covariance in the center region. The new function form is shown with the green dashed line in Figure 1, and listed below.

$$V(\theta) = 0.000292 \exp(-\theta/12^\circ) + 0.000292 \exp(-\theta/0.25^\circ), \quad (1)$$

θ indicates the angular separation between pairs of sources. The first term in the right part of eq. (1) is the fitted exponential function from Lindgren et al. (2021) (the black dashed line in Figure 1), while the second one is our additional term to account for the increase of covariance near the center (see the dotted-green line of Figure 1).

Figure 1 details how this covariance function fit to the angular covariance of proper motion from high precision quasar from Lindgren et al. (2021), as well as comparing to the fitting with single exponential function from Lindgren et al. (2021). The new fitting function of eq. (1) fit the covariance well for both large scale and central regions.

2.2 Robustness of GC Proper Motions

To have a clean sample with reliable astrometric measurements of the PM, we follow the recommendations of Fabricius et al. (2021): (1) renormalised unit weight error (RUWE) < 1.2. (2) asymmetric_excess_noise < 1.0. (3) ipd_gof_harmonic_amplitude < 0.1 (4)

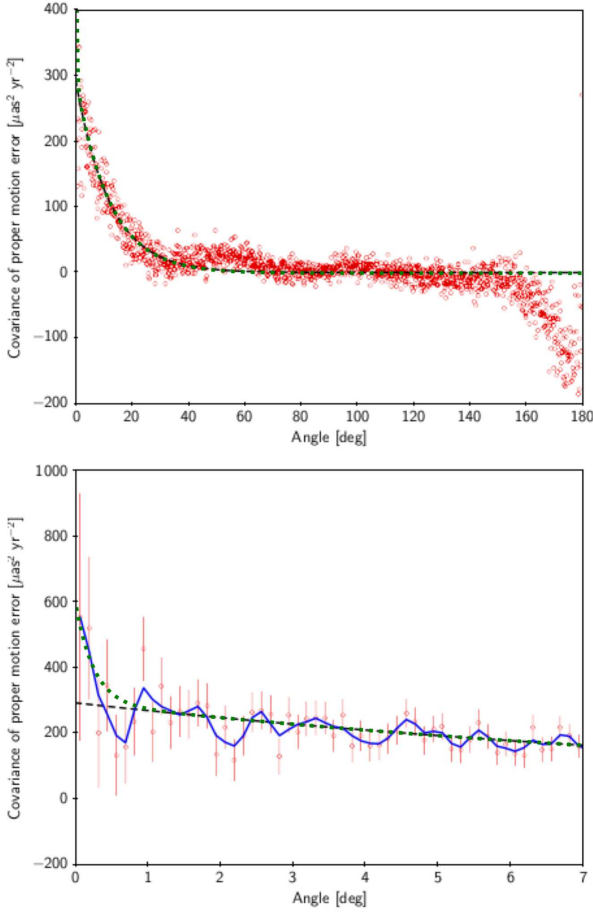


Figure 1. The covariance of proper motion of data in *Gaia* EDR3. This figure is from Figure 15 of Lindegren et al. (2021), except adding the new fitting curve (the dotted-green line) from eq. 1. The open red circles are individual estimates and the black dash-line is an exponential fitting. The top panel shows the large separation, while the bottom panel shows results for small separation angle. The individual estimates and the fitted black-dash line are from Lindegren et al. (2021). The blue-solid line indicates the smoothed covariance values from Lindegren et al. (2021). The green dashed line is our modified fitting to the exponential fitted result as shown by eq (1).

$\text{ipd_frac_multi_peak} < 2$ (5) the corrected excess factor (C_{corr}) within 3σ following Riello et al. (2021).

Figure 2 compare our measured proper motion, its associated uncertainties and correlation coefficient, and the internal dispersion with that from *Gaia* DR2 from Vasiliev (2019b).

The first two panels in the top-left compare the proper motion of μ_α^* and μ_δ from DR2 and EDR3 and they correlate well. In the first two panels in the bottom-left we show the absolute differences of proper motion as a function of μ_α^* and μ_δ , respectively. The absolute difference in proper motion is reasonably small, in most cases lower than 0.1 mas/yr.

In the two panels in the top-right, we compare the measured uncertainties of proper motions. The errors in EDR3 are systematic smaller than that from DR2 by about a factor of 2, which is fully consistent with Gaia Collaboration et al. (2020).

The third panel in the bottom row compares the correlated coefficients. The coefficients are well correlated, which shows that the correlation coefficients do not change too much even though the error of PM have decreased a factor of 2. The last panel of the bottom row compares the internal dispersion. The internal dispersion

are correlated between DR2 and EDR3, which probability indicate that this method has well resolved the intrinsic dispersion for each cluster.

After finishing this work, we notice Vasiliev & Baumgardt (2021) have measured the PM for GCs with *Gaia* EDR3 with an updated method comparing to Vasiliev (2019b) with a more strict selection criteria to clean the data. We have compared their results with ours (Figure 3) and find that it would not introduce significant differences in the final results as discussed in Appendix B.

3 DATA USED TO CONSTRAIN MW MASS MODELING

Besides GCs, here we describe other kinematic data set used to constrain the dynamic models for Milky Way.

3.1 Circular velocity from *Gaia* DR2

The rotation curve (RC) of the disk has been estimated by various tracers. By using the accurate proper motion from *Gaia* DR2 combining with precise spectrophotometric parallax from APOGEE DR16, Eilers et al. (2019) have derived disk RC for Galactocentric distance of $5 \leq R \leq 25$ kpc with high precision for ~ 23000 red giants. They have applied Jeans equation after assuming an axisymmetric gravitational potential to obtain this measurement. This result has been found consistent with measurement from Classic Cepheids (Mróz et al. 2019; Ablimit et al. 2020).

The precise distance and proper motion have led to the most precise RC derived to date (Eilers et al. 2019), i.e., with much smaller error bars than that of former studies. Eilers et al. (2019) have also analyzed systematic errors from various assumption. As mentioned by Jiao et al. (2021) that summing up all errors will dilute the significance of RC. Therefore, following Jiao et al. (2021) we added the systematic error of the cross-term in the radial and vertical velocity to the total error budgets. We noticed that this precise RC data have already been used to estimate MW mass Karukes et al. (2020).

This data will provide constraints on the disk RC for our modeling.

3.2 Vertical force at $z = 1.1$ kpc

Piffl et al. (2014) showed that the vertical force brings an important constraint to the dark matter shape, which has been widely used in the literature for estimating the MW potential (Bovy 2015; Bovy et al. 2016; McMillan 2017; Hattori, Valluri & Vasiliev 2021). By using Jeans equation Kuijken & Gilmore (1991) measured vertical force, $K_{z,1.1\text{kpc}}$ at $z = 1.1$ kpc away from the disk. Bovy & Rix (2013) using SDSS/SEGUE data measured the vertical force $K_{z,1.1\text{kpc}}(R)$ as function of radius, which is used in our analysis. As mentioned by Hattori, Valluri & Vasiliev (2021) the RC of Eilers et al. (2019) provides the radial force constraint on the model, while the $K_{z,1.1\text{kpc}}(R)$ gives an independent constraint on the vertical direction.

4 MODELING

In the following sections, we describe how the modeling for the GC DF has been setup. We note the six GCs associated with Sagittarius galaxy (NGC 6715, Terzan 7, Terzan 8, Arp 2, Pal 12, and Whiting 1), which we have excluded in the analysis following Vasiliev

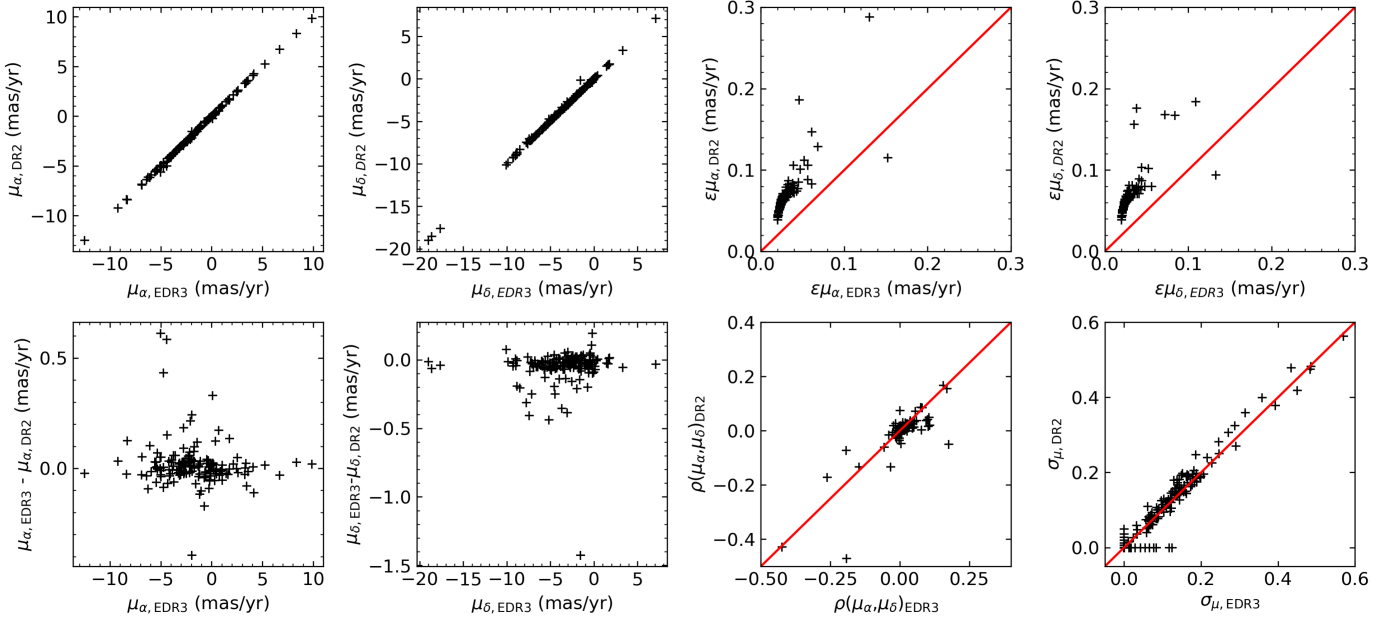


Figure 2. Comparing proper motion measurement between *Gaia* EDR3 of this work and DR2 from Vasiliev (2019b). The panels on the top row show the one-by-one comparison of proper motion in two direction μ_{α} , μ_{δ} , and their errors. The left two panels in the bottom row show the difference of proper motion in two directions as function of proper motions. The third panel of bottom row shows the comparison of correlation coefficient of proper motion. The fourth panel shows the internal dispersion of proper motion (for details please refer to Vasiliev (2019b)).

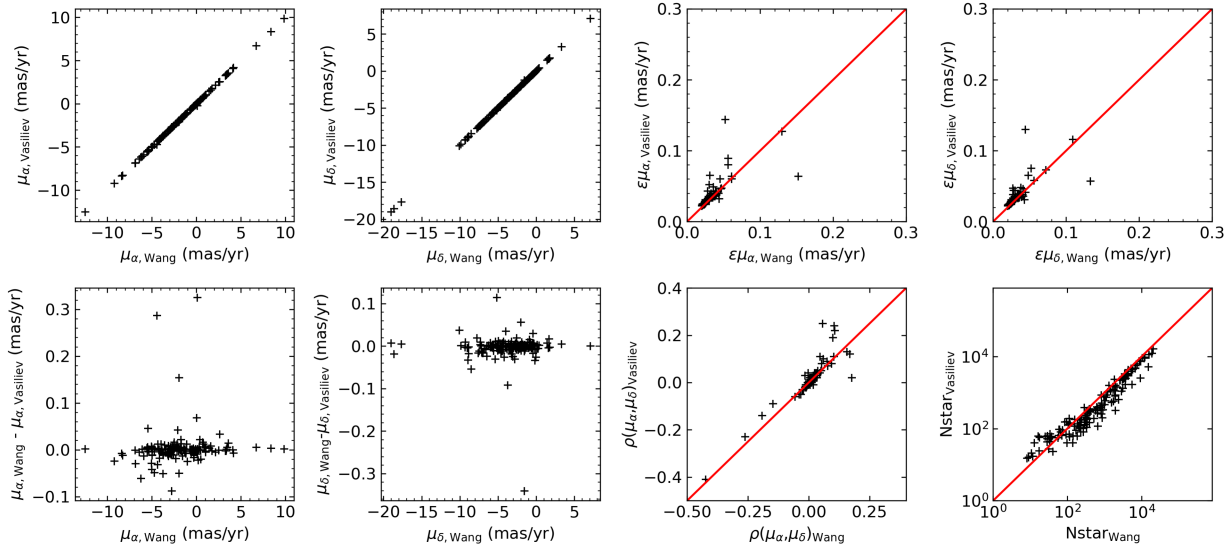


Figure 3. Comparing proper motion measurements in this work with Vasiliev & Baumgardt (2021) based on Gaia EDR3. The means for each panel are the same as Figure 2.

(2019b) and Myeong et al. (2019) and since they are clustering in the phase-space diagram. There could be other GCs associated with different accretion events (Massari, Koppelman & Helmi 2019) and they are included in current analysis. However, in section 6.3 we verify that unrelaxed substructures do not have significant effect on the final results, on the basis of an analysis made using the FIRE2 suite of simulations.

4.1 Models for the galactic gravitational potential

In this work we use axisymmetric Galactic potential $\Phi(R, z)$, which consist of baryon mass components and dark matter. In order to determine the dark matter mass profile, we first specify the adopted baryon mass model that follows McMillan (2017), and which include multi-components (a bulge, a thin and a thick stellar disc, an H I disc and a molecular gas disc).

Jiao et al. (2021) investigated different baryonic mass profiles to test the MW dark matter distribution. Here we prefer to adopt a

baryonic mass profile that also includes the gas contribution. Given the fact that baryons are not the dominant component, this should not alter our main conclusions.

4.1.1 The bulge

The stellar bulge component is modeled as McMillan (2017) as following:

$$\rho_b = \frac{\rho_{0,b}}{(1 + \frac{r'}{r_0})^\alpha} \exp \left[-\left(\frac{r'}{r_{\text{cut}}} \right)^2 \right], \quad (2)$$

where, in cylindrical coordinates,

$$r' = \sqrt{R^2 + \left(\frac{z}{q} \right)^2} \quad (3)$$

There is a bar in the central region of the MW, which introduces non-axisymmetric potential. In this work, we use the software *AGAMA* (Vasiliev 2019a) to deal with actions with Stäckel fudge method, which can only handle oblate axisymmetric potentials. Therefore, the central region is not expected to be well modelled. Following the literature (Vasiliev 2019b; Hattori, Valluri & Vasiliev 2021; Cautun et al. 2020), the parameters $r_0, \alpha, r_{\text{cut}}$, and a parameters are fixed during the modeling procedure, and their values are listed in Table 1. Following Cautun et al. (2020), the scale density of $\rho_{0,\text{bulge}}$ has a Gaussian prior value of $100 \pm 10 \text{ M}_\odot \text{ pc}^{-3}$.

4.1.2 The thin and thick stellar disk

The stellar disk is modeled by a thin and a thick disk component, which are both described by the following exponential profile:

$$\rho_d(R, z) = \frac{\Sigma_0}{2z_d} \exp \left(-\frac{|z|}{z_d} - \frac{R}{R_d} \right), \quad (4)$$

Here z_d denote the scale-height for the disk. Following McMillan (2017) we set z_d to be 0.3 and 0.9 kpc for thin and thick disk, and keep fixed during our modeling process. Σ_0 and R_d indicate the center surface density and scale-length for the disks. These two parameters for each disk components are not fixed, but fitted with Gaussian prior values. These prior values are from McMillan (2017), except for the thick disk scale-length (R_d), for which we adopt a value from 3.5 kpc from Bland-Hawthorn & Gerhard (2016) and Cautun et al. (2020). A 30% uncertainty is adopted for the Σ_0 and R_d during the fitting.

4.1.3 The molecular and atomic gas discs

The atomic (H_I) and molecular (H_2) gas disk parameters and form are adopted from McMillan (2017), and:

$$\rho_g(R, z) = \frac{\Sigma_0}{4z_d} \exp \left(-\frac{R_{\text{hole}}}{R} - \frac{R}{R_d} \right) \text{sech}^2 \left(\frac{z}{2z_d} \right), \quad (5)$$

These models are kept fix during the procedure. In the model, the mass of H_I is $1.1 \times 10^{10} \text{ M}_\odot$, and the molecular gas mass is around 10% of the H_I .

4.1.4 The dark matter halo

We chose two well-known and used mass profiles to get flexible the slope of DM density at outskirts, one follows Zhao (1996, hereafter called 'Zhao') and the other Einasto (1965, hereafter called 'Einasto').

There are five parameters in the Zhao's profile:

$$\rho(r) = \rho_{0,h} \left(\frac{r}{r_h} \right)^{-\gamma} \left[1 + \left(\frac{r}{r_h} \right)^\alpha \right]^{(\gamma-\beta)/\alpha}. \quad (6)$$

In the case of $\alpha = 1, \beta = 3$, and $\gamma = 1$ the profile corresponds to the NFW profile, which is widely used in the literature for representing dark matter halos. Comparing to the NFW profile, the Zhao's profile has more flexibility.

For the Einasto profile, we adopt:

$$\rho(r) = \rho_{0,h} \exp \left[\left(-\frac{r}{r_h} \right)^{-\beta} \right] \quad (7)$$

There are three parameters in the Einasto profile, which has been argued to provide the best description of the dark matter profile (Gao et al. 2008; Bullock & Boylan-Kolchin 2017).

The determination of Galactic DM shape is important to constraint cosmological models. The shape of DM halo is triaxial (Jing & Suto 2002) in DM-only simulation, and this can be affected by the inclusion of baryonic component. Chua et al. (2019) using Illustris suite of simulation found that the DM halo has an oblate-axisymmetric shape with a minor to major ratio of 0.75 ± 0.15 . The MW dark halo shape has been measured with various methods. Wegg, Gerhard & Bieth (2019) used RR Lyrae stars and they found the flattening of DM halo $q = 1.00 \pm 0.09$, based on the axisymmetric Jeans equation. The GD-1 stream kinematics has been used to measured the Galactic DM shape, and Malhan & Ibata (2019) found $q = 0.82 \pm_{-0.13}^{+0.25}$, while Bovy et al. (2016) gave $q = 1.3 \pm_{-0.3}^{+0.5}$. Vasiliev, Belokurov & Erkal (2021) modeled the Sagittarius stream considering the effect of a massive LMC on the MW using an oblate DM halo, which becomes triaxial beyond 50 kpc. With axisymmetric Jeans equations, Loebman et al. (2014) considered SDSS halo stars and estimated the MW DM density flattening to be $q = 0.4 \pm 0.1$. Therefore, the large range of q from different observations leads us to use a large range of flattening parameters for the modeling.

During the modeling, the halo shape is not spherical, and we have let the halo shape parameter q free varying from 0.1 to 1, which corresponds to an oblate shape ($q \leq 1$). In current studies, we are limited to oblate halos, which is a restriction due to the *AGAMA* software (Vasiliev 2019a). The lower limit is set to avoid calculation divergence.

All of the parameters for the two dark matter halo profiles are free in our modeling. In Table 2 all free parameters of the modeling are listed. Even though halo parameters are limited to ranges listed in Table 2, we have checked the MCMC chains for each parameter to be sure that parameters have been explored in sufficiently large ranges, to ensure the absence of non-investigated solutions.

4.2 Distribution function

By assuming that the GC system is in dynamical equilibrium, the distribution function (DF) of GCs can be expressed in phase-space by a function of $f(\mathbf{J})$ with three actions, $\mathbf{J} = (J_r, J_z, J_\phi)$, where

Table 1. Parameters of baryon gravitational potential are fixed in the dynamical model.

	H _I disc	H ₂ disc	Units
Σ_0	53.1	2179.5	$M_\odot \text{ pc}^{-2}$
R_d	7.00	1.5	kpc
z_d	0.85	0.045	kpc
R_{hole}	4	12	kpc
	Stellar thin disc	Stellar thick disc	Units
z_d	0.3	0.9	kpc
	Stellar bulge	Units	
r_0	0.075	kpc	
r_{cut}	2.1	kpc	
α	1.8		
q	0.5		

J_r and J_z is the radial and vertical actions, and J_ϕ is the azimuthal action and equal to angular momentum in the z component.

There are evidences for two distinct GC populations, one being metal-rich and the other metal-poor and the former show rapid rotations and are concentrated in the center (Harris & Canerna 1979; Zinn 1985). Unlike Binney & Wong (2017) and Posti & Helmi (2019) using two components in the DF to model the distribution function of GCs, we use a double-power-law DF (Vasiliev 2019b). As shown in Vasiliev (2019b) this DF is flexible enough to describe both populations reasonably well, and the gain is to have less free parameters.

$$f(\mathbf{J}) = \frac{M}{(2\pi J_0)^3} \left[1 + \left(\frac{J_0}{h(\mathbf{J})} \right)^\eta \right]^{\Gamma/\eta} \left[1 + \left(\frac{g(\mathbf{J})}{J_0} \right)^\eta \right]^{-B/\eta} \times \left(1 + \tanh \frac{\kappa J_\phi}{J_r + J_z + |J_\phi|} \right). \quad (8)$$

where

$$g(\mathbf{J}) \equiv g_r J_r + g_z J_z + (3 - g_r - g_z) |J_\phi|, \\ h(\mathbf{J}) \equiv h_r J_r + h_z J_z + (3 - h_r - h_z) |J_\phi|$$

The dimensionless parameters (g_r, g_z, g_ϕ) and (h_r, h_z, h_ϕ) control the density shape and the velocity ellipsoid in the outer region and inner region (Posti et al. 2015; Das & Binney 2016; Das, Williams & Binney 2016; Vasiliev 2019a), respectively. g_i and h_i have been constrained by $\Sigma_i h_i = \Sigma_i g_i = 3$ (Vasiliev 2019a). In this way the degeneracy between g_i and h_i and J_0 will be broken (Das & Binney 2016; Das, Williams & Binney 2016). The power-law indices B and Γ are related to the outer and inner slope, while η determine the steepness of this two regime transition. The parameter κ controls the net rotation of the system, with $\kappa = 0$ being the non-rotation case, and $\kappa = \pm 1$ indicate the maximal rotation case. In the publicly released version of AGAMA (Vasiliev 2019a), J_ϕ is normalized by a fixed constant, which leads to a non-rotating core. Following Vasiliev (2019b) we have modified the publicly released software AGAMA, in the way that the J_ϕ is normalized by the value summarizing three actions and the rotation will be roughly constant at all energies. The total mass is the normalization parameter.

4.3 Error models for observables

Observations of the GC system are not error-free. In the following we consider Gaussian models for the error to associate the true quantities with observables and its errors. The six observables for

GCs are $\bar{u} = (l, b, s, v_{\text{los}}, \mu_\alpha^*, \mu_\delta)$, where (l, b) denote the Galactic longitude and latitude which are measured with high precision so their errors are neglected in the following analysis. The heliocentric distance is s and its error is not neglected. Following Vasiliev (2019b) we adopted a 0.046 percent uncertainty (correspond to 0.1 in distance modulus). v_{los} is the line-of-sight velocity, and its value is taken from the Table C1 of Vasiliev (2019b). The proper motion is derived from the above study, and the correlated uncertainties in $\mu = (\mu_\alpha^*, \mu_\delta)$ as well as the covariance matrix (Σ_μ) are taken into account.

In the following, a Gaussian function is used to associate the observables (\bar{u}) to their true value (u). The error models for the heliocentric distance and line-of-sight velocity are:

$$N(s|\bar{s}, \sigma_s) = \frac{1}{\sqrt{2\pi\sigma_s^2}} \exp \left[-\frac{(\bar{s} - s)^2}{2\sigma_s^2} \right], \quad (9)$$

$$N(v_{\text{los}}|\bar{v}_{\text{los}}, \sigma_{v_{\text{los}}}) = \frac{1}{\sqrt{2\pi\sigma_{v_{\text{los}}}^2}} \exp \left[-\frac{(\bar{v} - v)^2}{2\sigma_{v_{\text{los}}}^2} \right], \quad (10)$$

For the proper motions:

$$N(\mu|\bar{\mu}, \Sigma_\mu) = \frac{1}{2\pi|\Sigma_\mu|^{1/2}} \exp \left[-\frac{1}{2}(\mu - \bar{\mu})^T \Sigma_\mu^{-1} (\mu - \bar{\mu}) \right] \quad (11)$$

4.4 The Bayesian inference

With the Bayes theorem, we can determine the posterior distribution of the model parameters (M) given the data (D). From this posterior distribution, the model parameters and their credible regions are estimated.

$$\Pr(M|D) = \frac{\Pr(D|M) \times \Pr(M)}{\Pr(D)} \quad (12)$$

where $\Pr(D|M)$ is the likelihood of the data given the model parameters, $\Pr(M)$ is the prior probability ascribed to the set of parameters, and $\Pr(D)$ is a normalization factor. In the following, we show how the total likelihood is built from the model and the priors.

4.4.1 Likelihood for the GC distribution function

$$\ln \mathcal{L}_{\text{GCs}} = \sum_{i=1}^{N_{\text{clusters}}} \ln \frac{S(\bar{\mathbf{u}}_i) \int d^6 \mathbf{u} E(\bar{\mathbf{u}}_i|\mathbf{u}, M) f(\mathbf{u}|M) \left| \frac{\partial(\mathbf{u}, \mathbf{v})}{\partial \mathbf{u}} \right|}{\int d^6 \mathbf{u}' \int d^6 \mathbf{u} E(\mathbf{u}'|\mathbf{u}, M) f(\mathbf{u}|M) S(\mathbf{u}') \left| \frac{\partial(\mathbf{u}, \mathbf{v})}{\partial \mathbf{u}} \right|}. \quad (13)$$

where \mathbf{u}' indicates the true value of the observational vector. $E(\bar{\mathbf{u}}|\mathbf{u}, M)$ denotes the error model (see section 4.3) for the probability of observables ($\bar{\mathbf{u}}$), given a model M and the true values \mathbf{u} . $f(\mathbf{u}|M)$ indicates the probability that a GC has a true vector \mathbf{u} given a model M . $\left| \frac{\partial(\mathbf{u}, \mathbf{v})}{\partial \mathbf{u}} \right|$ is the Jacobian factor for transformation of coordinate system with value $s^4 \cos \delta$. Following Posti & Helmi (2019) and Vasiliev (2019b) we have neglected the selection function ($S(\mathbf{u})=1$) on the GCs, since it has little effect on the model parameter inference, as demonstrated by Binney & Wong (2017). In this case the integration in the denominator is the normalization factor, which is the total number of GCs and that is identical for each cluster. The integral in the numerator is calculated with Monte Carlo sampling technique with fixed sampling points

and a weighting value to reduce the noise (Binney & Wong 2017; Vasiliev 2019b; Hattori, Valluri & Vasiliev 2021; Das & Binney 2016; Das, Williams & Binney 2016; McMillan & Binney 2013).

4.4.2 Likelihood from the disk circular data

The precise rotation curves in the disk region have been derived by Eilers et al. (2019), which can provide constraints on the total potential and can help to break the degeneracy between baryonic and DM contributions to the potential. This motivate us to include rotation curve data into our modeling with the Bayesian theorem.

For a given set of model parameters, the circular rotation curve for a given radius R at the meridian plane ($z = 0$), can be derived from the following equation:

$$v_{\text{circle}}^{\text{model}}(R) = \left[R \left(\frac{\partial \Phi(R, z=0)}{\partial R} \right) \right]^{1/2}. \quad (14)$$

Following Hattori, Valluri & Vasiliev (2021), the sum of the logarithm of the likelihood for the observed rotation curve from Eilers et al. (2019) can be derived as :

$$\ln \mathcal{L}_{\text{circle}} = - \sum_{i=1}^{N_{\text{circle}}} \sqrt{2\pi} \sigma_i + \frac{1}{2} \left(\frac{v_{\text{circle}}(R_i) - v_{\text{circle}}^{\text{model}}(R_i)}{\sigma_i} \right)^2. \quad (15)$$

$v_{\text{circle}}^{\text{model}}(R_i)$ indicates the rotation curve at each radial position of the observation data as done by Eilers et al. (2019). $v_{\text{circle}}(R_i)$ and σ_i give the observed rotation curve and its associated uncertainties of measured rotation curve at different radius from Eilers et al. (2019) and Jiao et al. (2021).

4.4.3 Likelihood for the vertical force $K_{z,1.1\text{kpc}}$

For a given set of model parameters, the vertical force at position of $(R, z = 1.1\text{kpc})$ can be derived as it follows:

$$K_{z=1.1\text{kpc}}^{\text{model}}(R) = \left[- \frac{\partial \Phi(R, z=1.1\text{kpc})}{\partial z} \right]. \quad (16)$$

Using the G dwarfs data from SDSS/SEGUE survey (Lee et al. 2011), Bovy & Rix (2013) derived the vertical force at $z = 1.1\text{kpc}$ ($K_{z=1.1}(R_i)$) at several radii assuming different 'mono-abundance' population. By requiring that the spatial distribution and the vertical kinematics are consistent with the phase-space data of observations, they derived an independent gravitational potential and a three-integral action-based DF for each sub-population, from which they derived the K_z at different radii. With the observation data for the vertical force at $z = 1.1\text{kpc}$ ($K_{z=1.1}(R_i)$) at different radii R_i and their associated errors ($\sigma_{K_z}(R_i)$) from Bovy & Rix (2013), the sum of logarithmic likelihood is derived from the following:

$$\ln \mathcal{L}_{K_z} = - \sum_{i=1}^{N_{K_z}} \sqrt{2\pi} \sigma_{K_z}(R_i) + \frac{1}{2} \left(\frac{K_{z=1.1\text{kpc}}(R_i) - K_{z=1.1\text{kpc}}^{\text{model}}(R_i)}{\sigma_{K_z}(R_i)} \right)^2. \quad (17)$$

4.4.4 Total likelihood

We take a simple and reasonable assumption that given the model parameters, the above three observation data set are conditionally

independent, which do not provide additional information about each other. Then from the above derivation, the total logarithmic likelihood for a given set model parameters can be expressed as:

$$\ln \Pr(D|M) = \ln \mathcal{L}_{\text{GCs}} + \ln \mathcal{L}_{K_z} + \ln \mathcal{L}_{\text{circle}} \quad (18)$$

4.4.5 The Priors

In the Bayesian inference, we can put priors to constrain the amplitude of parameters. Our priors are listed in Table 2. The prior in the baryon gravitational potential is mostly taken from McMillan (2017), Deason et al. (2021), and Bland-Hawthorn & Gerhard (2016), and a Gaussian function is adopted for the prior function. For the parameters related to the dark matter profile and DF of GCs, the priors are set as uniform within the a reasonable ranges listed in Table 2. In the Cold Dark Matter (CDM), the dark matter halo follow a cuspy density profile with $\gamma \sim 1$ (NFW), however, the observed rotation curve of local spirals seems to be more consistent with core density profile with $\gamma \sim 0$. The core density profile is also reasonable for dwarf spheroidal galaxies and Low Surface Brightness (LSB). (see Di Matteo et al. 2008 for discussion). The situation become more complex if the dark matter profile is modified after the inclusion of baryons (Cautun et al. 2020), which results in the fact that neither NFW nor the generalized NFW succeeded to fit the MW rotation curve data. However Jiao et al. (2021) found that a nearly flat density core with Einasto profile is best for MW dark matter density profile, including baryons or not. Based on the above discussion, we decide to adopt non-informative flat priors for the dark matter profile parameters. For the parameters relevant to the DF of GCs, we chose uniform priors following the literature (Vasiliev 2019b; Posti & Helmi 2019; Binney & Wong 2017). We have visually checked the posterior distribution for the MCMC chains to be sure that the prior range is large enough and do not impose constraints on the parameters sampling.

4.5 Model parameter estimates

We use the Nelder-Mead method implemented in the python scipy package to maximize the above likelihood, and find the parameters with maximum-likelihood. By using these parameters as initial input values, we use Monte Carlo Markov Chain (MCMC) method to explore the parameter space, which is implemented in the EMCEE package (Foreman-Mackey et al. 2013). To be sure a converged results achieved with MCMC, we run $\sim 10 \times N_{\text{pars}}$ (where N_{pars} is the total number of free parameters) walkers for the modeling of the GC system, and $\sim 5 \times N_{\text{pars}}$ for the mock simulation data in section 6. The MCMC is ran for several thousand steps to be sure to achieve a converging result, and in the following analysis, the first half chain is discarded for the initial burn-in chain. We use the median value of the posterior distribution for the estimated results, and 68 percentile for the credible intervals. We point out that 68 percentile does not reflect a one σ error bar since the marginal posterior distribution is non-Gaussian.

5 RESULTS ON THE MW MASS

5.1 The posterior distribution of parameters

In this Section we examine the final results from analyzing the posterior distribution. To have an overall view about the estimated parameters of our modeling, we show the posterior distribution of the

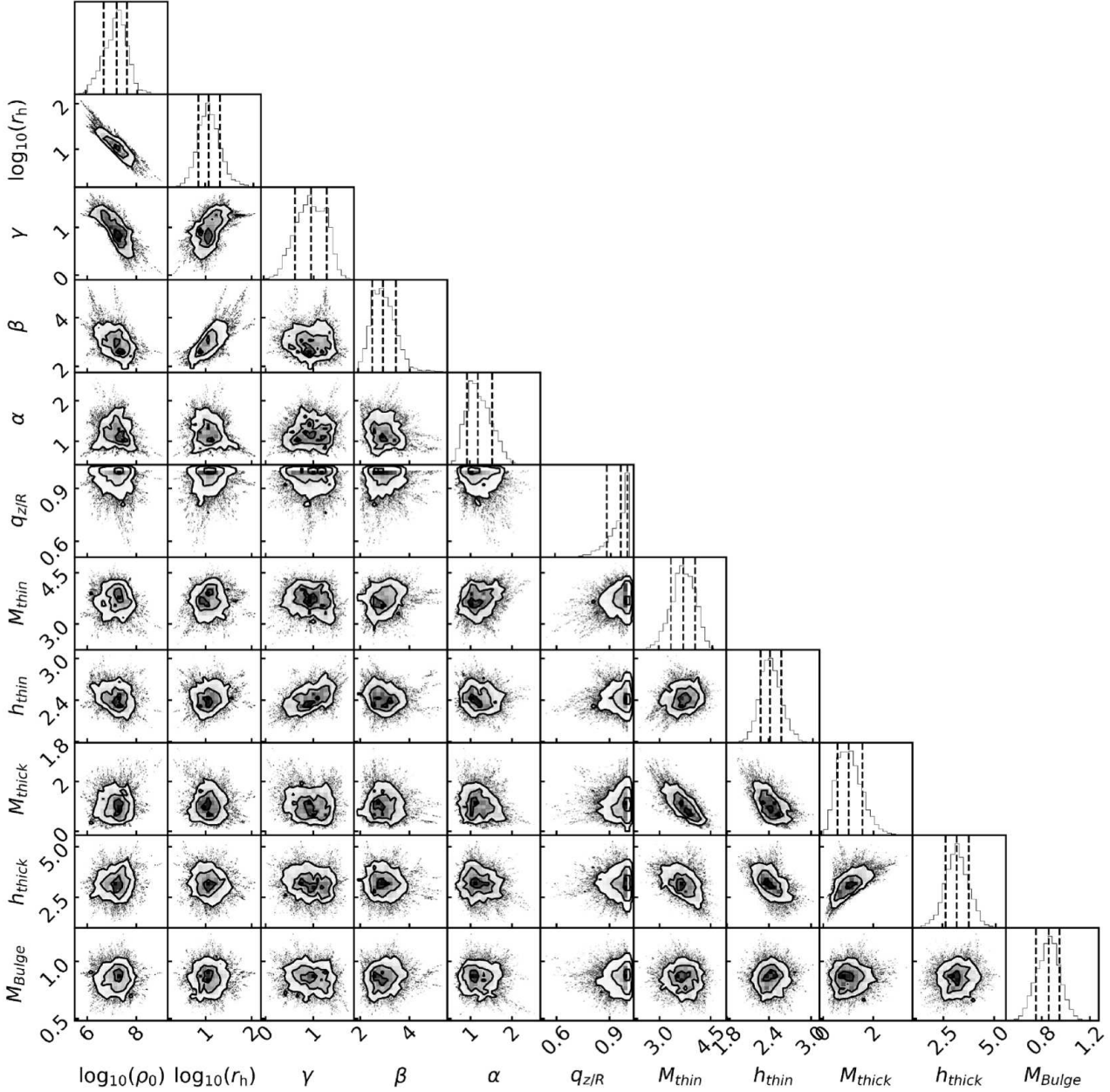


Figure 4. Posterior distribution of parameters for potential fields with model using the Zhao’s DM density profile (Eq.6). The parameters $\log \rho_0$, $\log a_{\text{scale}}$, γ , β and α , are for parameters of dark matter mass distribution. The parameters M_{thin} , M_{thick} , M_{bulge} are total mass for the thin and thick disk, and bulge components, with units in $10^{10} M_{\odot}$. The parameters h_{thin} , h_{thick} indicate the scale-length for thin and thick disk, respectively. Contour lines in each panel and the vertical lines in the marginal histograms show the 16%, 50%, 84% percentiles.

inferred parameters with Zhao DM density profile (Eq.6) in Figure 4 and 5. The posterior distribution of estimated parameters are separated into gravitational potential fields (Figure 4) and distribution function of GCs (Figure 5), respectively. The posterior distribution of parameters show that they converge well. The final results are listed in Table 2 in the last columns, with both the DM density profiles for Einasto (Eq.7) and Zhao (Eq.6) models.

5.2 Fits of the observational data

Even though we have adopted the similar modeling method as in Vasiliev (2019b), there are two major differences with them. First, we have used Gaia EDR3 which improves the uncertainties by a factor of 2. Second, we have added two important tight constraints by imposing the model to fit both the MW RC and the vertical force data. It would be useful to check how the DF different to that of Vasiliev (2019b).

Following Vasiliev (2019b) we have derived from our posterior distribution the velocity structure variation and the axis ratio of

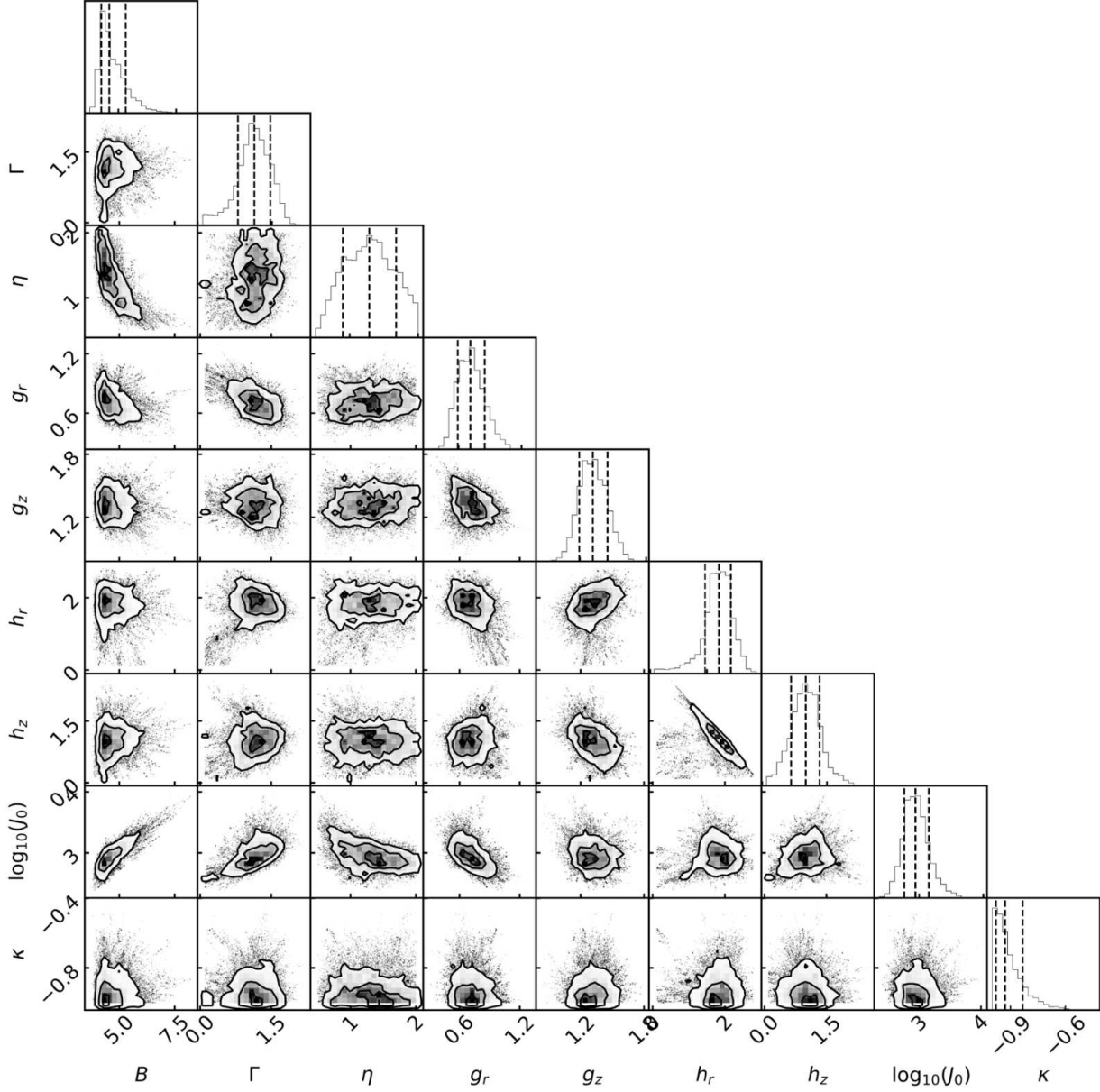


Figure 5. Posterior distribution of parameters of DF (eq. 8) of GCs with model using the Zhao’s DM density profile (Eq.6). The parameters B and Γ related to the outer and inner slopes of DF, while η determine the steepness of transition. The dimensionless parameters g_r, g_z, h_r, h_z control the density shape and the velocity ellipsoid in the outer and inner region. The inner and outer regions are separated with actions J_0 . κ that control the rotation. Contour lines in each panel and the vertical lines in the marginal histograms show the 16%, 50%, 84% percentiles.

GCs as a function of the radius as it is shown in Figure 6. The velocity anisotropic parameter β varies with radius, being isotropic in the center and radially dominated at the outskirts. The axis ratio q increases with radius, which is consistent with the disk component in the inner region (Binney & Wong 2017).

Figure 6 shows our modeling results of GCs and compare them to that of Vasiliev (2019a). The velocity dispersion, anisotropic parameter, and axis ratio of GCs are found to be very similar, however the radial velocity dispersion shows large discrepancy at $r > 10$ kpc from one to the other study.

Figure 7 compares the vertical force $K_{z=1.1\text{kpc}}$ from the ob-

served data (Bovy & Rix 2013) and that derived from our posterior distribution. The model reproduce well the observed vertical force.

5.3 The Milky Way Rotation Curve

Figure 8 shows the RCs derived from our new modeling with Zhao’s DM density profiles (Eq.6, the red-line and shaded region). The derived RC is fitting well the disk RC of Eilers et al. (2019), for which velocities are much lower than that predicted by McMillan (2017). The RC from Zhao’s DM profile is consistent with the recent results of Vasiliev, Belokurov & Erkal (2021) and Eadie & Jurić (2019), as shown in Fig.8. Cautun et al. (2020) have

Table 2. The model parameters used in our modeling. The best derived values are shown with median and 68 percentile of the posterior distribution. Gaussian prior functions have been used for baryon model parameters, while flat prior has been adopted for all the other parameters. The ranges of parameters in the prior have been chosen which are large enough without imposing constraints on the parameters sampling with MCMC when checking the MCMC chains. The low limit of out slope (β) for DM profile in Zhao is set to 2, and 0 for Einasto profile.

Parameters	Symbol	Units	Prior	Best fitting values	
				Einasto halo	Zhao's halo
Gravitational Potential					
<i>Baryon gravitational Potential</i>					
bulge density	$\rho_{0,\text{bulge}}$	$\text{M}_\odot \text{ pc}^{-3}$	100 ± 10	$94.64^{+9.35}_{-9.76}$	$95.20^{+9.90}_{-11.79}$
thin disc density	$\Sigma_{0,\text{thin}}$	$\text{M}_\odot \text{ pc}^{-2}$	900 ± 270	$1057.50^{+87.71}_{-89.42}$	$1003.12^{+134.77}_{-130.70}$
thick disc density	$\Sigma_{0,\text{thick}}$	$\text{M}_\odot \text{ pc}^{-2}$	183 ± 55	$167.76^{+57.40}_{-54.09}$	$167.93^{+60.09}_{-54.06}$
thin disc scale length	R_{thin}	kpc	2.5 ± 0.5	$2.39^{+0.11}_{-0.11}$	$2.42^{+0.15}_{-0.13}$
thick disc scale length	R_{thick}	kpc	3.5 ± 0.7	$3.20^{+0.52}_{-0.54}$	$3.17^{+0.56}_{-0.54}$
<i>DM density profile</i>					
DM density	ρ_0	$\text{M}_\odot \text{ kpc}^{-3}$	$0 < \log_{10} \rho_0 < 15$	$9.29^{+0.20}_{-0.21}$	$7.19^{+0.38}_{-0.51}$
DM scale length	r_h	kpc	$-2 < \log_{10} r_h < 4.5$	$-1.40^{+0.26}_{-0.26}$	$1.07^{+0.24}_{-0.21}$
Inner slope	γ	–	$0 < \gamma < 3$	–	$0.95^{+0.31}_{-0.32}$
steepness	α	–	$0 < \alpha < 20$	–	$1.19^{+0.33}_{-0.25}$
Outer slope	β	–	$2^{\text{Zhao}}, 0^{\text{Eina}} < \beta < 20$	$0.32^{+0.02}_{-0.02}$	$2.95^{+0.51}_{-0.41}$
axis ratio (z/R)	q	–	$0.1 < q < 1$	$0.97^{+0.03}_{-0.06}$	$0.95^{+0.04}_{-0.07}$
Distribution function of GCs					
slopeOut	B	–	$3.2 < B < 10$	$5.03^{+1.88}_{-0.64}$	$4.61^{+0.71}_{-0.35}$
slopeIn	Γ	–	$0.1 < \Gamma < 2.8$	$1.23^{+0.26}_{-0.28}$	$1.14^{+0.32}_{-0.34}$
steepness	η	–	$0.5 < \eta < 2.0$	$1.08^{+0.52}_{-0.37}$	$1.29^{+0.39}_{-0.39}$
coefJrOut	g_r	–	$0.1 < g_r < 2.8$	$0.65^{+0.12}_{-0.13}$	$0.71^{+0.14}_{-0.12}$
coefJzOut	g_z	–	$0.1 < g_z < 2.8$	$1.32^{+0.11}_{-0.13}$	$1.32^{+0.13}_{-0.12}$
coefJrIn	h_r	–	$0.1 < h_r < 2.8$	$1.86^{+0.31}_{-0.29}$	$1.81^{+0.32}_{-0.37}$
coefJzIn	h_z	–	$0.1 < h_r < 2.8$	$1.01^{+0.29}_{-0.30}$	$1.01^{+0.32}_{-0.34}$
J_0	J_0	–	$-2 < \log_{J_0} < 7$	$3.08^{+0.45}_{-0.22}$	$2.94^{+0.21}_{-0.18}$
rotFrac	κ	–	$-1 < \kappa < 1$	$-0.94^{+0.08}_{-0.04}$	$-0.93^{+0.10}_{-0.05}$
Derived quantities					
bulge mass	$M_{\star,\text{bulge}}$	10^{10} M_\odot	–	$0.85^{+0.09}_{-0.08}$	$0.86^{+0.09}_{-0.11}$
thin disc mass	$M_{\star,\text{thin}}$	10^{10} M_\odot	–	$3.79^{+0.28}_{-0.30}$	$3.69^{+0.34}_{-0.37}$
thick disc mass	$M_{\star,\text{thick}}$	10^{10} M_\odot	–	$1.03^{+0.47}_{-0.39}$	$1.05^{+0.53}_{-0.45}$
M_{200}	$M_{200; \text{MW}}$	10^{11} M_\odot	–	$5.73^{+0.76}_{-0.58}$	$7.84^{+3.08}_{-1.97}$
R_{200}	$R_{200; \text{MW}}$	kpc	–	$170.7^{+7.2}_{-5.9}$	$189.5^{+22.1}_{-17.4}$
V_{escaped} at sun	$v_{\text{esc},\odot}$	km s^{-1}	–	$495.5^{+11.2}_{-9.7}$	$528.3^{+55.3}_{-31.4}$
DM density at sun	$\rho_{\text{DM},\odot}$	GeV cm^{-3}	–	$0.34^{+0.02}_{-0.01}$	$0.34^{+0.02}_{-0.02}$

also fitted the disk RC of Eilers et al. (2019) considering the baryon contraction effect. They considered constraints from dwarf satellites based on Callingham et al. (2019), which results in a higher value of RC at outskirts than our value.

5.4 Escaped velocity and DM density at solar position

Accurately deriving the DM mass density profile means that we can make predictions on the escaped velocity and the DM density at solar position, and compare them with different measurements in the literature. Figure 9 shows the probability distribution function

(PDF) of the escaped velocity at solar position. Our value is consistent with the most recent results on the escaped velocity measurement (Deason et al. 2019; Necib & Lin 2021). Figure 10 show the PDF of dark matter density at solar position. The new results is consistent with results from Read (2014).

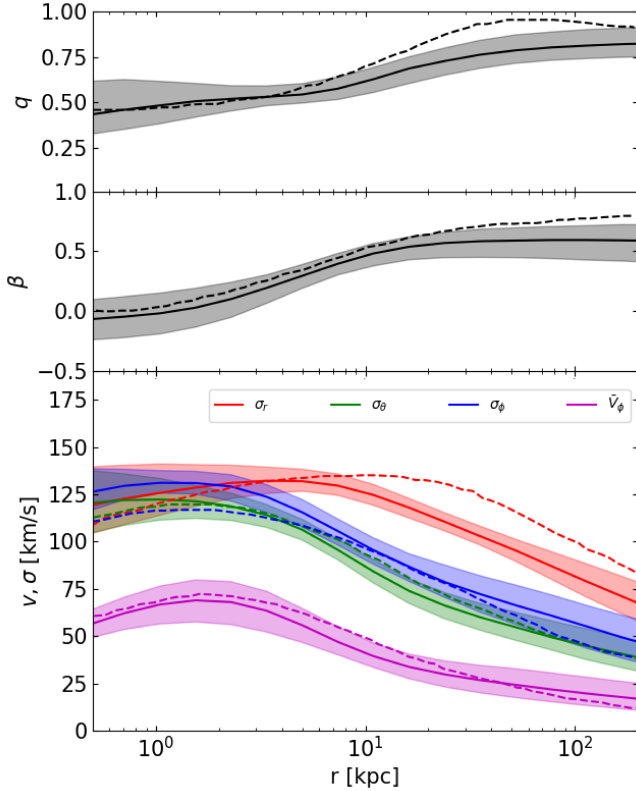


Figure 6. Physical quantities estimated from ensemble of models from MCMC runs in function of radius. The solid lines are the mean values estimated from MCMC models, while the shaded regions indicate the 68 per cent credible regions. Top panel: the axial ratio ($q = z/R$) of GCs spatial density profile varied as function of radius. Middle panel: the velocity anisotropic parameter $\beta = 1 - (\sigma_\theta^2 + \sigma_\phi^2)/(2\sigma_r^2)$ in function of the radius. Bottom panel: the velocity dispersions in three directions and the mean azimuthal velocity as function of the radius. For comparison, the dotted-lines in each panel shows the results from Vasiliev (2019a).

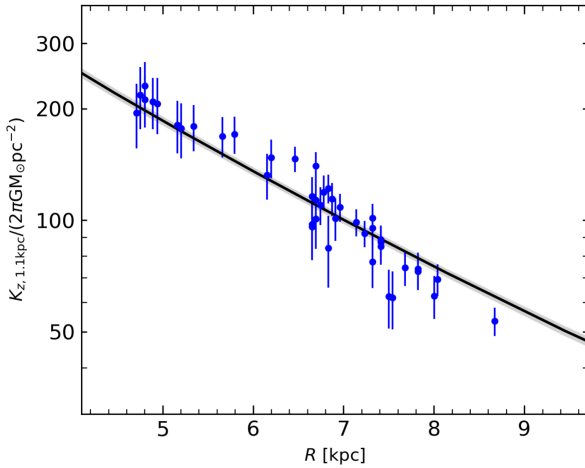


Figure 7. The vertical force at $z = 1.1$ kpc as function of radius. The blue solid circle and error bars are from the observation measurements by Bovy & Rix (2013), and the black line and shaded region indicate the estimated and 68 percentile of posterior distribution of our model.

6 DISCUSSION

6.1 Influence of the a priori choice of the MW mass density profile

The MW baryon content is relatively well known, though there are still variations by $\sim 30\%$ for each component from one study to another (see Poulidas, Di Matteo & Haywood 2017). Our method recovers these uncertainties by letting varying by similar amount the baryonic components.

The DM content of the MW is less constrained since it is found highly dependent on the choice of tracers. Here we have used very robust tracers, which are stars embedded into the disk and GCs, as well as constraints from the vertical force. For the later, we even consider in the Appendix A the alternative for which some (Crater) could be dwarf galaxy instead, or not bound (Pyxis). Our goal is to keep as large as possible the range of DM profile for the halo. This is why we have chosen both Zhao and Einasto profiles. The first one is a generalization of the NFW and of the generalized NFW profiles that have been often used to fit DM halos. The second is acknowledged to reproduce better the DM halo density profile coming from simulations (Navarro et al. 2004; Dutton & Macciò 2014; Gao et al. 2008). It has also the advantage to be parameterized by only 3 parameters against 5 for the Zhao profile, however it may become a disadvantage if more complex DM distribution is required, for e.g., fitting the MW mass profile in presence of a massive LMC.

Jiao et al. (2021) have shown that NFW and of the generalized NFW dark matter profiles may be biased in favor of high values for the total MW mass when compared to results using the Einasto profile. Results of our paper based on the Zhao’s DM profile indeed provide higher mass values than that from Einasto DM profile, which may confirm the Jiao et al. (2021) results. Nevertheless we prefer to keep the whole range of possibilities in fitting the DM component of the MW, and to consider the whole range of MW masses provided by these two kinds of excellent models in reproducing the DM.

A recent study shows that the DM profile could be changed during the process of the baryon contraction in the center region, which result in profile deviate from NFW (Cautun et al. 2020). We do not think this can alter our conclusions, because Jiao et al. (2021) showed that the Einasto model is able to reproduce a contracting halo.

6.2 A massive LMC may introduce disequilibrium

There has been many clues that a massive LMC $\sim 10^{11} M_\odot$ passing by MW could have non-negligible effects on the MW (Erkal, Belokurov & Parkin 2020; Petersen & Peñarrubia 2021; Conroy et al. 2021), and on the track of stellar streams (Vasiliev, Belokurov & Erkal 2021; Erkal et al. 2019; Koposov et al. 2019). For example, several halo tracers have shown velocity gradients that are predicted by a massive LMC model (Petersen & Peñarrubia 2021).

However, the fact that the LMC could very massive is still under discussion. For example, GC distributions show no significant velocity shift (Erkal, Belokurov & Parkin 2020). Conroy et al. (2021) found that halo K giants show a local wake and a Northern over-density, which can be explained by the passage of a massive LMC. However, as they showed a reasonable tilted triaxial

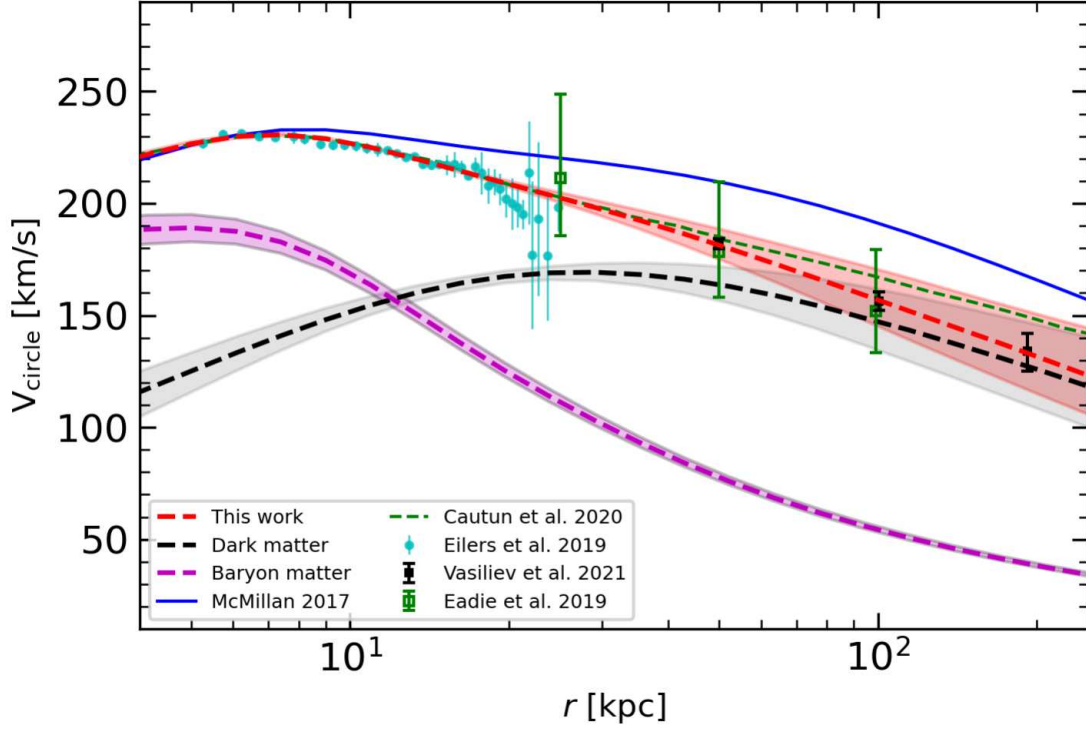


Figure 8. It compares rotation curves derived from posterior distribution of our models with literature. The Zhao’s dark matter model is used. The shaded region indicate the 68 percentile. The black dashed-line indicates the contribution from dark matter, while the magenta dashed-line shows the contribution from baryon matter.

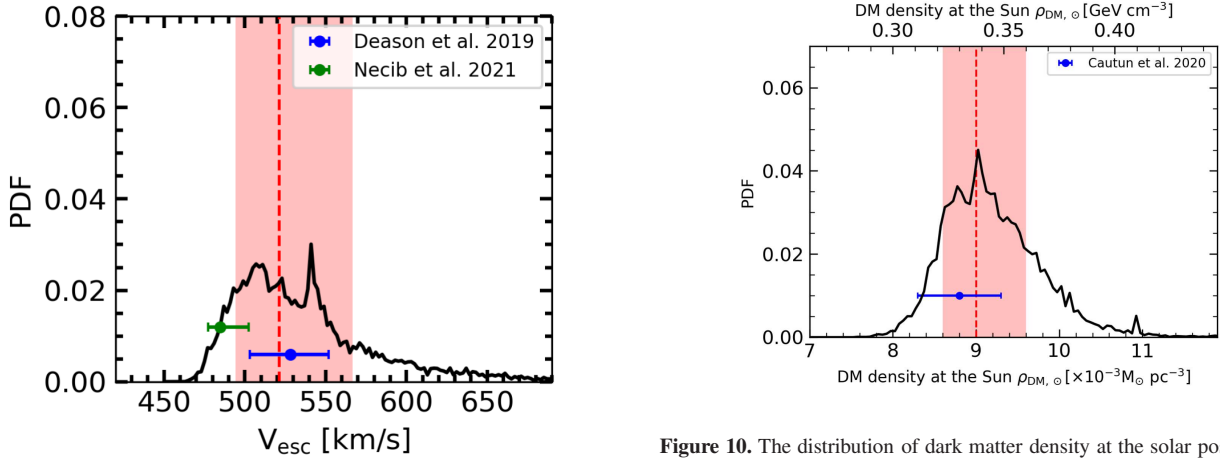


Figure 9. The posterior distribution of the escaped velocity at the solar position for the Zhao DM density model. The red-dashed line and shaded region indicate the median and 68 percentiles for the distribution, and these values are listed in Table 2

Figure 10. The distribution of dark matter density at the solar position for the Spheroid model. The median and associated 68 percentile of the posterior distribution from our MCMC runs are indicated by red-dashed line and shaded regions, and these values are listed in Table 2.

halo model can explain this phenomenon equally well. It has often acknowledged that the LMC is at first-passage to the MW (Kallivayalil et al. 2013). The splendid Magellanic Stream has been well reproduced under the frame of ‘ram-pressure plus collision’ model (Hammer et al. 2015; Wang et al. 2019), which reproduces

well the neutral gas morphology including its structure into two filaments, the observed hot ionized distribution, as well as the very peculiar stellar morphology of the SMC. This model requires the total mass of LMC to be less than $2 \times 10^{10} M_{\odot}$, which is almost one decade smaller than that of a very massive LMC.

To test the effect of LMC on the final MW mass measurement, we make a simulation to test how a massive LMC passing by MW may affect mass estimates. We follow the same method of

Vasiliev, Belokurov & Erkal (2021) and we have built the pair of MW and LMC. Vasiliev, Belokurov & Erkal (2021) built models of the MW and LMC interaction to investigate the effect on the Sagittarius stream track. Their MW model consist of a stellar disk, bulge, and dark matter halo. The dark matter halo have axis-symmetric or triaxial-symmetric shape. For simplicity, we have used a spherical dark matter model. We also introduce a light gas component, which does not produce an essential effect on the total mass profile, but that is used to generate test particles for reproducing the modeled rotation curve. The LMC has a truncated NFW profile with total mass $1.5 \times 10^{11} M_{\odot}$. We notice that the model of Vasiliev et al (2021) does not reproduce the MW RC (Eilers et al. 2019) and that it overestimates rotational velocities by about 5%. We then slightly scale down the MW mass value to match the rotation curve. We note that these small change have little effects on the final results. We also remark that this modeling does not intent to reproduce whole full properties of the MW and massive LMC. Instead, its goal is to gauge the effect of a massive LMC to the constraints from the MW RC. Details on the structure of the pairs of LMC and MW and on the simulations of their interactions can be found in Vasiliev, Belokurov & Erkal (2021).

The LMC starts from 427 kpc away and is launched to reach the current observed position, at about 50 kpc to the MW center. The top row of Figure 11 shows the final velocity vector map of MW dark matter particles. The massive LMC induces a strong disequilibrium for MW system in which the systematic velocities are changed at different positions, which indicates that correcting the systematic effect is complex.

Bearing in mind that the GC system shows no systematic velocity shift (Erkal, Belokurov & Parkin 2020), we build a mock observational sample from the simulated samples (Figure 11). We randomly select the mock GC sample by using dark matter halo particles, adjusting their number to that of GCs.

With the simulated (mock) GC samples, we have perturbed the true value ($s, v_{los}, \mu_{\alpha}^*, \mu_{\delta}$) according to the uncertainties of the observed GCs. The distance uncertainty is $\sim 5\%$. The mean errors of line-of-sight velocity of the GCs are very small and fixed to 1.8 km/s. The mean proper motion errors in both directions are ~ 0.03 mas/yr. The covariance correlation coefficient are set by a randomly selected from Gaussian distribution with $\sigma = 0.06$ and zero mean value following observations.

To mimic the observed rotation curve of Eilers et al. (2019), we have used the mean streaming velocity of gas particle, which has less velocity dispersion, and then less asymmetric drift correction. We also measured the vertical force at 1.1 kpc above the disk, which mimics the observation data (Bovy & Rix 2013). The RC and vertical force data in the simulated model have similar fraction errors as observations.

With the mimicked observation data in hand, we have used the action-based DF method listed above to model the gravitational field on the simulated data. Figure 12 compares the final result to the true values. The green dashed-line shows the true rotation curve of input MW without LMC perturbation. The blue dashed-line indicates the rotation curve derived with $V_c = \sqrt{\frac{GM(<r)}{r}}$ assuming a spherical mass distribution for the overall contribution of MW and LMC. The black-dashed line indicates the RC derived with $\sqrt{R \frac{\partial \Phi}{\partial R}}$. The mass estimate with the spherical mass distribution assumption is less accurate, because of the non-spherical shape of disk mass distribution and of the LMC contribution. The red-dashed line shows the results with action-based DF modeling. The contribution from the massive LMC is well recovered by the

action-based PDF modeling, as shown by the slight bump of RC at ~ 50 kpc in Figure 12. The introduction of a massive LMC leads to overestimate the mass at large radius ($r > 100$ kpc). The black and cyan symbols show the gas streaming velocity in the center region for both without and with LMC perturbation, both of these rotation velocities are consistent with each other. This indicates that the central region within the disk is much less affected by the massive LMC than the outer halo region, which provides us further confidence in using of rotation curve data from Eilers et al. (2019).

6.3 Effect of substructures

A recent discovery shows that the MW halo consists of many substructures, for example, the Sagittarius streams which contribute large fraction of halo stars (10 \sim 15 per cent; Deason et al. 2021; Deason, Belokurov & Sanders 2019). The big merger event, *Gaia* Sausage or *Gaia* Enceladus, which occurred 10 Gyr ago also contributes to a large fraction of inner halo stars (Belokurov et al. 2018; Helmi et al. 2018; Naidu et al. 2021)

In order to test the effect of these unrelaxed substructure effect on the measurement, we use the model m12m of the FIRE2 Latte cosmological hydrodynamic simulations suite, which produces a realistic Milky-Way-like galaxy, including many unrelaxed substructures (Wetzel et al. 2016; Hopkins 2015; Hopkins et al. 2018). From this model, we generate the mock GC sample. We select stars from model 'm12m' with age older than 10 Gyr, using them to represent the GC samples. From the simulated model we derive the rotation curve and vertical force at 1.1 kpc and add observational errors as in Hattori, Valluri & Vasiliev (2021). With our modeling machine we derive the final rotation curve and compare it with input data as shown in Fig. 13. The unrelaxed substructures in the halo result only in moderate fluctuations of the rotation curve.

6.4 MW total mass and comparison with literature and implication for cosmology

The total mass is critical for many cosmological satellite problem, for instance, "too-big-to-fail" (Boylan-Kolchin, Bullock & Kaplinghat 2011; Wang et al. 2012), and missing satellite problem. Our measurement for the mass of the MW is $7.84^{+3.08}_{-1.97} \times 10^{11} M_{\odot}$ and $5.8^{+0.81}_{-0.68} \times 10^{11} M_{\odot}$, after using the Zhao and the Einasto model for DM, respectively. Appendix discusses how these values can be slightly affected by different ways in using the GC sample, i.e., by removing or not Crater and Pyxis.

Figure 14 compares the total MW mass measured in this work with recent results by using *Gaia* DR2 and EDR3. This figure is an update of Fig. 5 of Wang et al. (2020), in which the results are grouped on the basis of the different methods used to estimate the MW total mass. Our range of estimates is at the low end of MW mass, which may alleviate the tension of the 'too-big-to fail' problem. Recent studies have suggested that only three MW satellites (MCs and Sagittarius dwarf, see Wang et al. 2012) could inhabit in sub-halos with their value of V_{\max} larger than a threshold $V_{th} \sim 30$ km/s, which is defined by Boylan-Kolchin, Bullock & Kaplinghat (2011) as the massive failure threshold. Wang et al. (2012) used Λ CDM cosmological simulations and showed that only ~ 5 per cent of halos with mass $M_{halo} \sim 2 \times 10^{12} M_{\odot}$ have three or fewer sub-haloes with $V_{\max} > 30$ km/s, while this fraction increases to ~ 70 per cent for a MW mass of $7.5 \times 10^{11} M_{\odot}$. The total mass of MW in

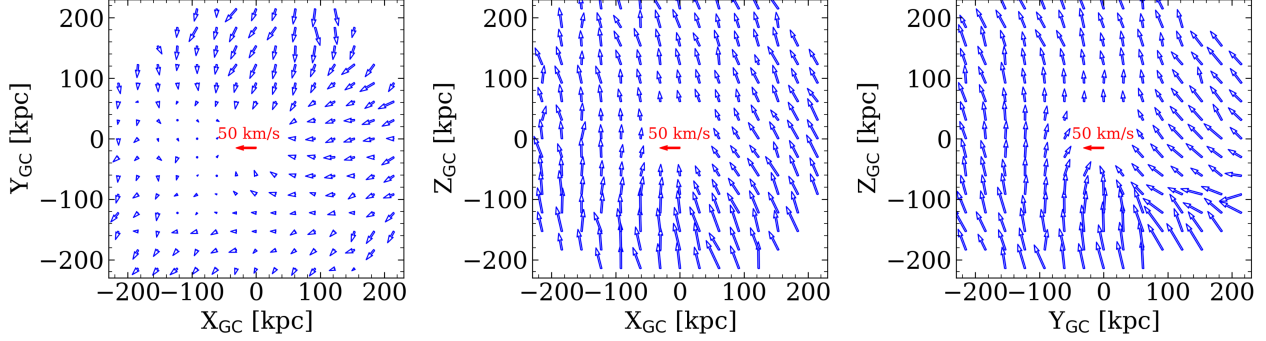


Figure 11. The simulated velocity vectors maps for dark matter halo particles at different positions after the perturbation of a massive LMC ($1.5 \times 10^{11} M_{\odot}$) passing by. Only particles outside the disk region ($r > 20$ kpc) are shown.

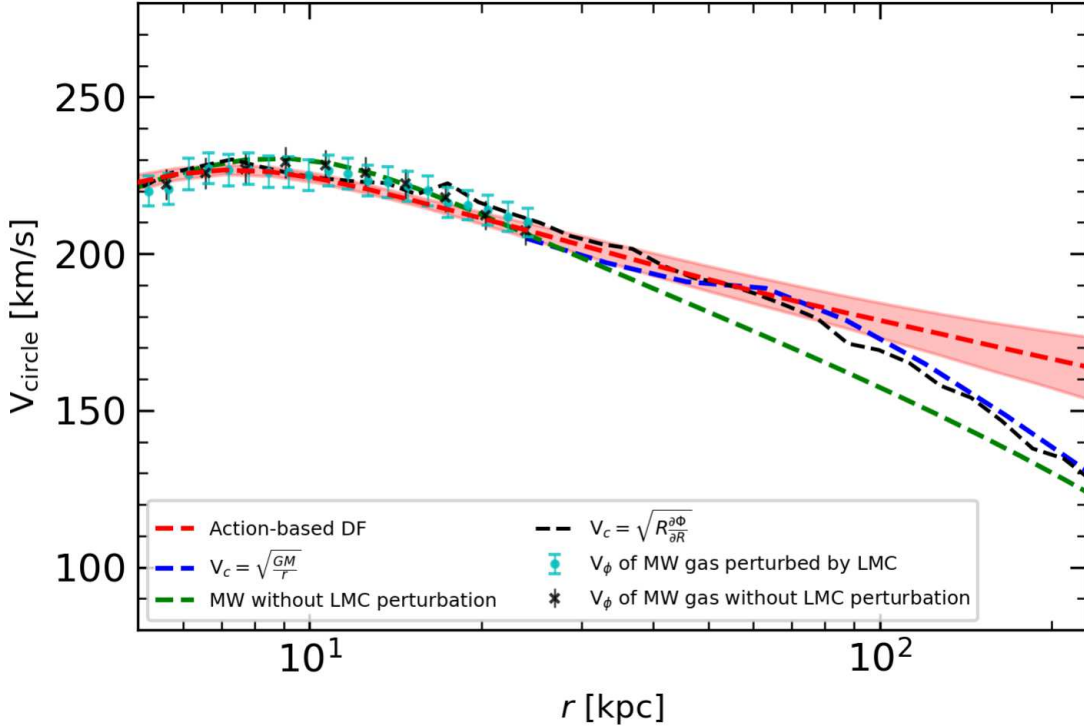


Figure 12. It compares the measured RC for the simulated GCs with observed values. The green-dashed line show the input RC of MW without LMC perturbation. The blue-dashed line shows the rotation curve for the MW perturbed by LMC calculated with $V_c = \sqrt{\frac{GM(<r)}{r}}$, which include the contribution by LMC. The black crosses show the measured streaming velocity of gas without LMC perturbation. The cyan-dots show the streaming velocity of gas disk after LMC perturbation. The red-dash line shows the RC recovered by the action-based distribution method with shaded region indicate 68 per cent credible regions. The black-dashed line indicates the RC derived with $\sqrt{R \frac{\partial \Phi}{\partial R}}$ after LMC perturbation.

our measurement naturally includes the contribution for LMC in our measurement, since the contribution by LMC has been added into the measured velocity for GCs. By assuming the LMC mass is $1.5 \times 10^{11} M_{\odot}$, leads to a MW total mass of $6.34 \times 10^{11} M_{\odot}$.

7 CONCLUSION

Using *Gaia* EDR3 data, we derive proper motions for about 150 MW GCs. When comparing their proper motions with that from *Gaia* DR2, errors decrease by about a factor 2, which is consistent with the *Gaia* data reduction analysis.

With the newly derived proper motions for the MW GCs and by combining them to the constraints from the rotation curve from 5 to 25 kpc and from the vertical force measurements, we have

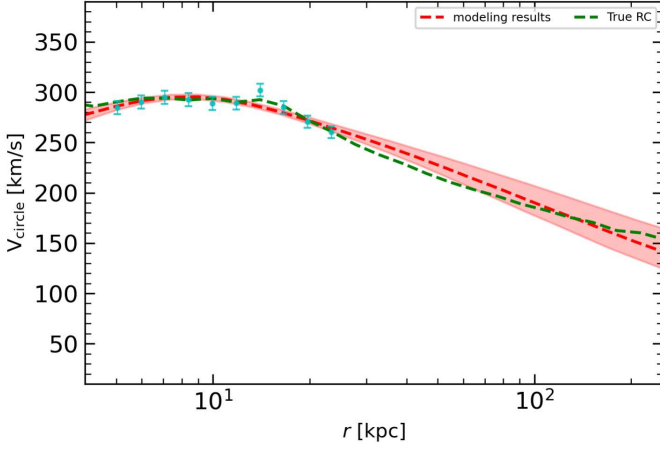


Figure 13. Comparing modeling results with mock MW-like of model 'm12m' of FIRE2, which is a MW-like galaxy from cosmological hydrodynamic simulations with unrelaxed substructures. The green-dashed line indicates the true rotation curve for the model 'm12m', while the cyan points show the rotation curve data with random errors added following observational errors. The red-dashed line and pink shaded region denote the modeling results and 68 percent credible region from the models of MCMC run.

built dynamical models for the MW using the action-based distribution function. From the new dynamical model we have derived the rotation curve and the mass profile for MW, and have compared them with recent results based on Gaia data. The local dark matter density and local escaped velocity are all consistent with literature values.

We have used mock simulation data to test the robustness of our results. Firstly, we consider the perturbation of a possible massive LMC passing by MW, which results in the reflex motion of halo stars with velocity intensities and directions modified at different positions (Figure 11). By modeling mock GCs system from the simulations with action-based DF and comparing with the input value, we found the modeling can well recover the input rotation curve value including the contribution from the massive LMC ($1.5 \times 10^{11} M_{\odot}$) within 100 kpc. At large distances, this model overestimates the rotation curve ~ 20 percent at 200 kpc. Secondly, we consider the effect of unrelaxed substructures on the results. We have used the realistic cosmological hydrodynamic simulations from FIRE2 Latter simulation data suite. The model "m12m" produce a MW-like galaxy with unrelaxed substructures. From the data model, we select stars with age older than 10 Gyr to build mock GCs system. The unrelaxed substructure results in the final rotation curve fluctuating around its true value by about 10 percent.

In this paper we have chosen the most objective view in adopting baryonic and DM mass, by avoiding a priori against or for a given modeling. It results that the total mass of the MW ranges from $5.36^{+0.81}_{-0.68} \times 10^{11} M_{\odot}$ to $7.84^{+3.08}_{-1.97} \times 10^{11} M_{\odot}$, which significantly narrows the previous ranges for the MW mass in the literature.

ACKNOWLEDGMENTS

We thanks the referee helpful comments, which have significantly improved the manuscript. The computing task was carried out

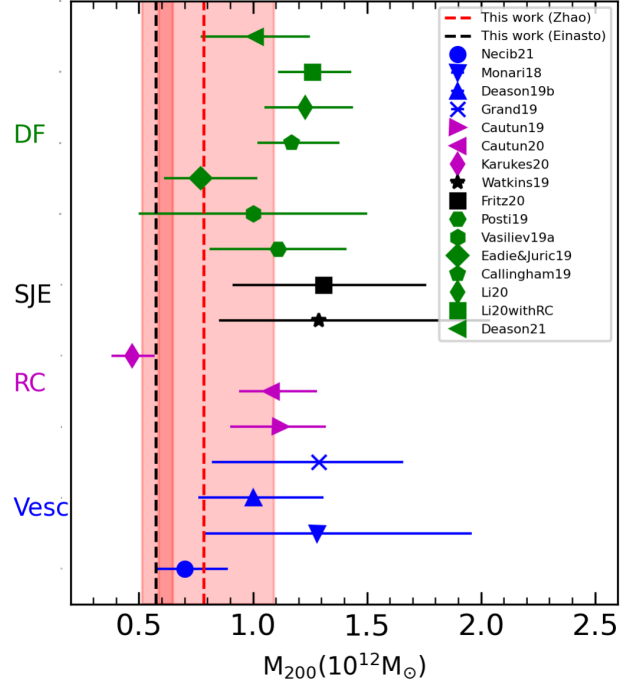


Figure 14. Comparing MW total mass results measured in this work with that made use of *Gaia* DR2 or EDR3. This figure is an update of Fig.5 in Wang et al. (2020). Different methods has been labeled with different color. DF(distribution function): Posti & Helmi (2019); Vasiliev (2019b); Eadie & Jurić (2019); Callingham et al. (2019); Li et al. (2020); Deason et al. (2021), Spherical Jeans Equation (SJE): Watkins et al. (2019); Fritz et al. (2020), RC: Karukes et al. (2020); Cautun et al. (2019, 2020), Escaped Velocity(Vesc): Necib & Lin (2021); Monari et al. (2018); Deason et al. (2019); Grand et al. (2019). Red-dashed line indicates result of this work for Zhao's DM profile, and black-dashed line show result from Einasto's DM profile. The pink shaded region shows the 68 percentile credible intervals.

on the HPC cluster at China National Astronomical Data Center (NADC). NADC is a National Science and Technology Innovation Base hosted at National Astronomical Observatories, Chinese Academy of Sciences. This work is supported by Grant No. 12073047 of the National Natural Science Foundation of China.

This work has made use of data from the European Space Agency (ESA) mission *Gaia* (<http://www.cosmos.esa.int/gaia>), processed by the *Gaia* Data Processing and Analysis Consortium (DPAC, <http://www.cosmos.esa.int/web/gaia/dpac/consortium>). Funding for the DPAC has been provided by national institutions, in particular the institutions participating in the *Gaia* Multilateral Agreement.

DATA AVAILABILITY

The data underlying this article will be shared on reasonable request to the corresponding author.

REFERENCES

Ablimit I., Zhao G., Flynn C., Bird S. A., 2020, *ApJL*, 895, L12

- Belokurov V., Erkal D., Evans N. W., Koposov S. E., Deason A. J., 2018, *MNRAS*, 478, 611
- Binney J., 2020, in *Galactic Dynamics in the Era of Large Surveys*, Valluri M., Sellwood J. A., eds., Vol. 353, pp. 101–108
- Binney J., Wong L. K., 2017, *MNRAS*, 467, 2446
- Bland-Hawthorn J., Gerhard O., 2016, *ARA&A*, 54, 529
- Bonifacio P., Caffau E., Zaggia S., François P., Sbordone L., Andrievsky S. M., Korotin S. A., 2015, *A&A*, 579, L6
- Bovy J., 2015, *ApJS*, 216, 29
- Bovy J., Bahmanyar A., Fritz T. K., Kallivayalil N., 2016, *ApJ*, 833, 31
- Bovy J., Rix H.-W., 2013, *ApJ*, 779, 115
- Bowden A., Belokurov V., Evans N. W., 2015, *MNRAS*, 449, 1391
- Boylan-Kolchin M., Bullock J. S., Kaplinghat M., 2011, *MNRAS*, 415, L40
- Bullock J. S., Boylan-Kolchin M., 2017, *ARA&A*, 55, 343
- Callingham T. M. et al., 2019, *MNRAS*, 484, 5453
- Cautun M. et al., 2020, *MNRAS*, 494, 4291
- Cautun M., Deason A. J., Frenk C. S., McAlpine S., 2019, *MNRAS*, 483, 2185
- Cautun M., Hellwing W. A., van de Weygaert R., Frenk C. S., Jones B. J. T., Sawala T., 2014, *MNRAS*, 445, 1820
- Chua K. T. E., Pillepich A., Vogelsberger M., Hernquist L., 2019, *MNRAS*, 484, 476
- Conroy C., Naidu R. P., Garavito-Camargo N., Besla G., Zaritsky D., Bonaca A., Johnson B. D., 2021, *Nature*, 592, 534
- Cui X.-Q. et al., 2012, *Research in Astronomy and Astrophysics*, 12, 1197
- Das P., Binney J., 2016, *MNRAS*, 460, 1725
- Das P., Williams A., Binney J., 2016, *MNRAS*, 463, 3169
- Deason A. J., Belokurov V., Sanders J. L., 2019, *MNRAS*, 490, 3426
- Deason A. J. et al., 2021, *MNRAS*, 501, 5964
- Deason A. J., Fattahi A., Belokurov V., Evans N. W., Grand R. J. J., Marinacci F., Pakmor R., 2019, *MNRAS*, 485, 3514
- Di Matteo P., Bournaud F., Martig M., Combes F., Melchior A. L., Semelin B., 2008, *A&A*, 492, 31
- Dutton A. A., Macciò A. V., 2014, *MNRAS*, 441, 3359
- Eadie G., Jurić M., 2019, *ApJ*, 875, 159
- Eilers A.-C., Hogg D. W., Rix H.-W., Ness M. K., 2019, *ApJ*, 871, 120
- Einasto J., 1965, *Trudy Astrofizicheskogo Instituta Alma-Ata*, 5, 87
- Erkal D. et al., 2019, *MNRAS*, 487, 2685
- Erkal D., Belokurov V. A., Parkin D. L., 2020, *MNRAS*, 498, 5574
- Fabricius C. et al., 2021, *A&A*, 649, A5
- Foreman-Mackey D., Hogg D. W., Lang D., Goodman J., 2013, *PASP*, 125, 306
- Fritz T. K., Di Cintio A., Battaglia G., Brook C., Taibi S., 2020, *MNRAS*, 494, 5178
- Fritz T. K. et al., 2017, *ApJ*, 840, 30
- Gaia Collaboration, Brown A. G. A., Vallenari A., Prusti T., de Bruijne J. H. J., Babusiaux C., Biermann M., 2020, *arXiv e-prints*, arXiv:2012.01533
- Gao L., Navarro J. F., Cole S., Frenk C. S., White S. D. M., Springel V., Jenkins A., Neto A. F., 2008, *MNRAS*, 387, 536
- Gibbons S. L. J., Belokurov V., Evans N. W., 2014, *MNRAS*, 445, 3788
- Grand R. J. J., Deason A. J., White S. D. M., Simpson C. M., Gómez F. A., Marinacci F., Pakmor R., 2019, *MNRAS*, 487, L72
- Hammer F., Yang Y., Arenou F., Wang J., Li H., Bonifacio P., Babusiaux C., 2020, *ApJ*, 892, 3
- Hammer F., Yang Y. B., Flores H., Puech M., Fouquet S., 2015, *ApJ*, 813, 110
- Harris W. E., Canterna R., 1979, *ApJL*, 231, L19
- Hattori K., Valluri M., Vasiliev E., 2021, *MNRAS*, 508, 5468
- Helmi A., Babusiaux C., Koppelman H. H., Massari D., Veljanoski J., Brown A. G. A., 2018, *Nature*, 563, 85
- Hopkins P. F., 2015, *MNRAS*, 450, 53
- Hopkins P. F. et al., 2018, *MNRAS*, 480, 800
- Jiao Y., Hammer F., Wang J. L., Yang Y. B., 2021, *A&A*, 654, A25
- Jing Y. P., Suto Y., 2002, *ApJ*, 574, 538
- Kafle P. R., Sharma S., Lewis G. F., Bland-Hawthorn J., 2012, *ApJ*, 761, 98
- Kafle P. R., Sharma S., Lewis G. F., Bland-Hawthorn J., 2014, *ApJ*, 794, 59
- Kallivayalil N., van der Marel R. P., Besla G., Anderson J., Alcock C., 2013, *ApJ*, 764, 161
- Karukes E. V., Benito M., Iocco F., Trotta R., Geringer-Sameth A., 2020, *JCAP*, 2020, 033
- Koposov S. E. et al., 2019, *MNRAS*, 485, 4726
- Kuijken K., Gilmore G., 1991, *ApJL*, 367, L9
- Küpper A. H. W., Balbinot E., Bonaca A., Johnston K. V., Hogg D. W., Kroupa P., Santiago B. X., 2015, *ApJ*, 803, 80
- Lee Y. S. et al., 2011, *ApJ*, 738, 187
- Li H., Hammer F., Babusiaux C., Pawłowski M. S., Yang Y., Arenou F., Du C., Wang J., 2021, *arXiv e-prints*, arXiv:2104.03974
- Li Z.-Z., Qian Y.-Z., Han J., Li T. S., Wang W., Jing Y. P., 2020, *ApJ*, 894, 10
- Lindgren L. et al., 2018, *A&A*, 616, A2
- Lindgren L. et al., 2021, *A&A*, 649, A2
- Loebman S. R. et al., 2014, *ApJ*, 794, 151
- Malhan K., Ibata R. A., 2019, *MNRAS*, 486, 2995
- Massari D., Koppelman H. H., Helmi A., 2019, *A&A*, 630, L4
- McMillan P. J., 2017, *MNRAS*, 465, 76
- McMillan P. J., Binney J. J., 2013, *MNRAS*, 433, 1411
- Monari G. et al., 2018, *A&A*, 616, L9
- Moore B., Ghigna S., Governato F., Lake G., Quinn T., Stadel J., Tozzi P., 1999, *ApJL*, 524, L19
- Mróz P. et al., 2019, *ApJL*, 870, L10
- Myeong G. C., Vasiliev E., Iorio G., Evans N. W., Belokurov V., 2019, *MNRAS*, 488, 1235
- Naidu R. P. et al., 2021, *arXiv e-prints*, arXiv:2103.03251
- Navarro J. F. et al., 2004, *MNRAS*, 349, 1039
- Necib L., Lin T., 2021, *arXiv e-prints*, arXiv:2102.02211
- Petersen M. S., Peñarrubia J., 2021, *Nature Astronomy*, 5, 251
- Piffl T. et al., 2014, *MNRAS*, 445, 3133
- Posti L., Binney J., Nipoti C., Ciotti L., 2015, *MNRAS*, 447, 3060
- Posti L., Helmi A., 2019, *A&A*, 621, A56
- Pouliasis E., Di Matteo P., Haywood M., 2017, *A&A*, 598, A66
- Read J. I., 2014, *Journal of Physics G Nuclear Physics*, 41, 063101
- Riello M. et al., 2021, *A&A*, 649, A3
- Riley A. H. et al., 2019, *MNRAS*, 486, 2679
- Sofue Y., 2012, *PASJ*, 64, 75
- Vasiliev E., 2019a, *MNRAS*, 482, 1525
- Vasiliev E., 2019b, *MNRAS*, 484, 2832
- Vasiliev E., 2019c, *MNRAS*, 489, 623
- Vasiliev E., Baumgardt H., 2021, *MNRAS*, 505, 5978
- Vasiliev E., Belokurov V., Erkal D., 2021, *MNRAS*, 501, 2279
- Voggel K., Hilker M., Baumgardt H., Collins M. L. M., Grebel E. K., Husemann B., Richtler T., Frank M. J., 2016, *MNRAS*,

- 460, 3384
Wang J., Frenk C. S., Navarro J. F., Gao L., Sawala T., 2012, MNRAS, 424, 2715
Wang J., Hammer F., Yang Y., Ripepi V., Cioni M.-R. L., Puech M., Flores H., 2019, MNRAS, 486, 5907
Wang W., Han J., Cautun M., Li Z., Ishigaki M. N., 2020, Science China Physics, Mechanics, and Astronomy, 63, 109801
Watkins L. L., van der Marel R. P., Sohn S. T., Evans N. W., 2019, ApJ, 873, 118
Wegg C., Gerhard O., Bieth M., 2019, MNRAS, 485, 3296
Wetzel A. R., Hopkins P. F., Kim J.-h., Faucher-Giguère C.-A., Kereš D., Quataert E., 2016, ApJL, 827, L23
York D. G. et al., 2000, AJ, 120, 1579
Zhao G., Zhao Y.-H., Chu Y.-Q., Jing Y.-P., Deng L.-C., 2012, Research in Astronomy and Astrophysics, 12, 723
Zhao H., 1996, MNRAS, 278, 488
Zinn R., 1985, ApJ, 293, 424

APPENDIX A: DYNAMICAL MODELLING ON GCS WITH EINASTO PROFILE

Figure A1 shows the result of the dynamical modeling of the GC system based on the Einasto DM profile (Eq.7). The Einasto DM profile results in a lower mass estimate at $r > 100$ kpc compared to that from Zhao's DM profile (Figure 8). Fig.A2 and Fig.A3 show the posterior distribution for gravitational and DF parameters with Einasto's DM profile.

We also notice that there are two GCs, Crater and Pyxis, for which properties are still disputed. It is not fully clear whether Crater is a dwarf or a GC (Bonifacio et al. 2015; Voggel et al. 2016), and Fritz et al. (2017) argued that Pyxis is accreted from a disrupted dwarf. We tested our results by excluding the two GCs from our samples, and found the MW total mass are $6.77^{+3.00}_{-1.74} \times 10^{11} M_{\odot}$ and $5.36^{+0.81}_{-0.68} \times 10^{11} M_{\odot}$ with Zhao and Einasto profile, respectively. These values are lower than that derived with the full samples (Table 2). We note that the multi-population in the samples have no significant effect on our results as being test with our FIRE2 simulation. The proper motion of Pyxis in the *Gaia* DR2 and EDR3 (this work and Vasiliev 2019b; Vasiliev & Baumgardt 2021) is smaller than that used in Fritz et al. (2017), which corresponds to velocity decrease by ~ 70 km/s and making Pyxis bound to the MW system. Therefore, including it in the samples is reasonable.

APPENDIX B: DYNAMICAL MODELLING ON GCS WITH DATA FROM VASILIEV ET AL. 2021B

In order to check how the results changing with PM results of Vasiliev & Baumgardt (2021), we also run our code on GCs data from Vasiliev & Baumgardt (2021) as shown in Fig.B1. The results is very similar to that with GC PMs derived in this work. The total mass of MW with the data of Vasiliev & Baumgardt (2021) is $8.27^{+3.59}_{-2.14} \times 10^{11} M_{\odot}$, which is slightly larger than the result with our GCsdata, but still within the error bars.

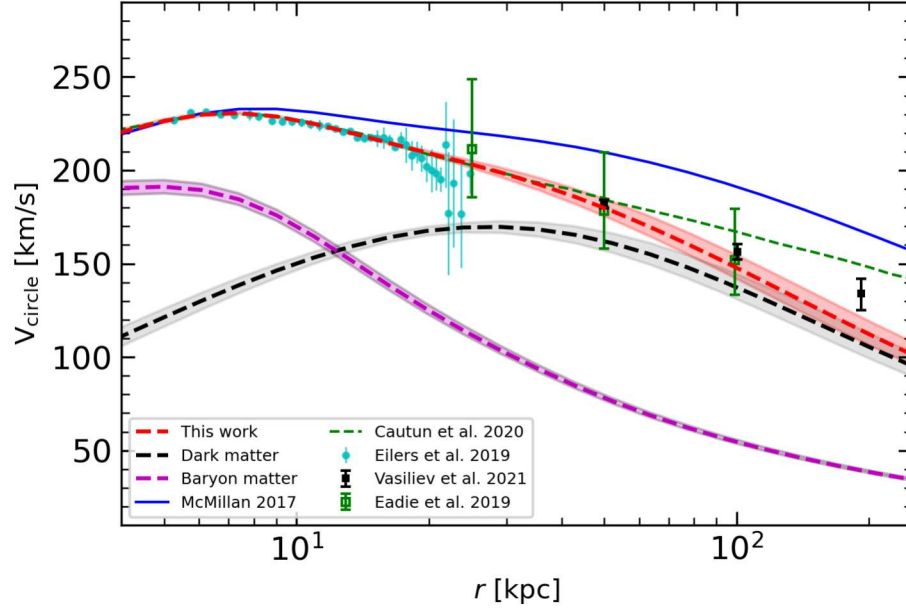


Figure A1. It compares rotation curves derived from posterior distribution of our models with literature. Here the Einasto dark matter profile is used. The shaded region indicate the 68 percentile.

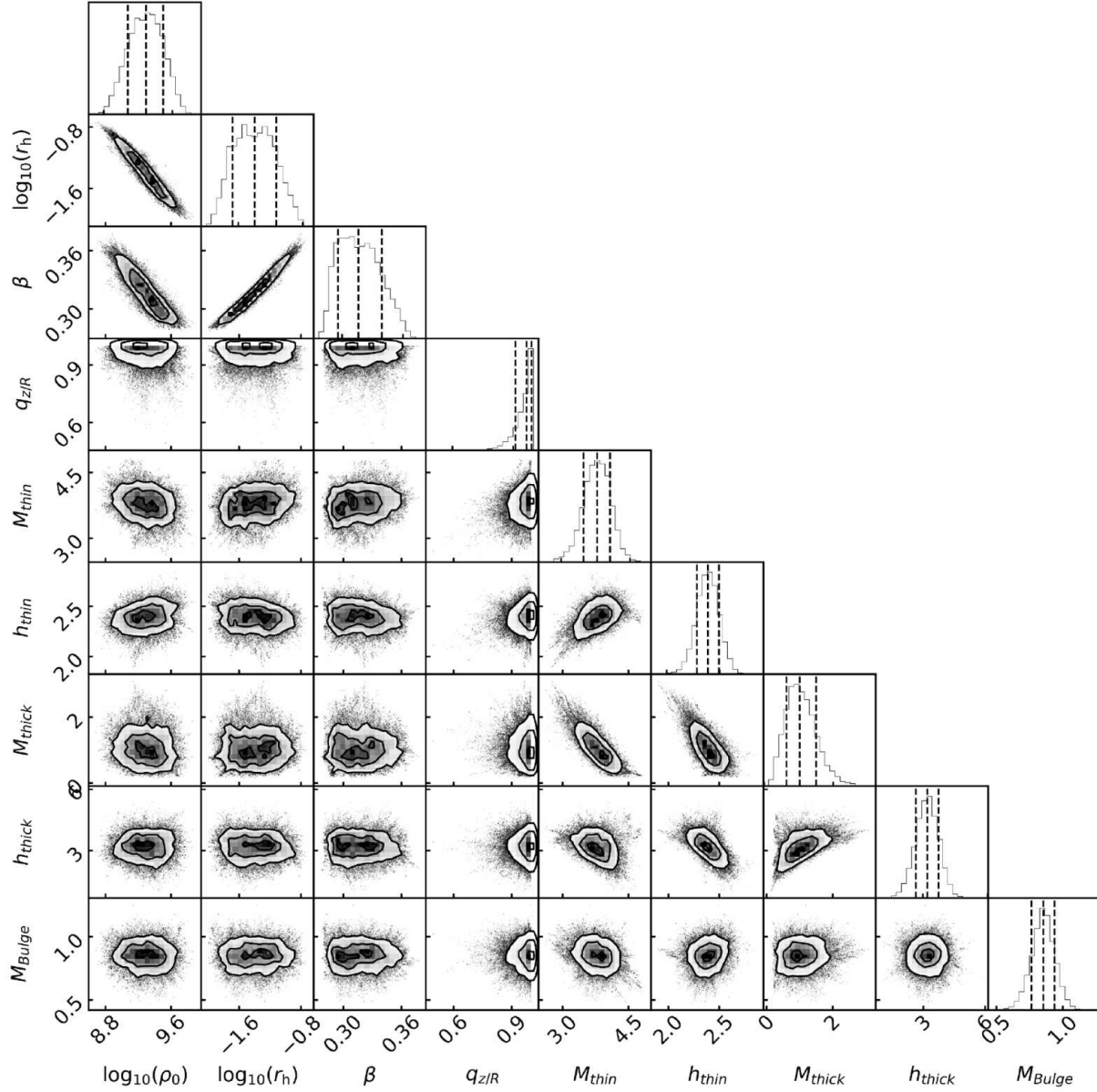


Figure A2. Posterior distribution of parameters for potential fields with model using the Einasto's DM density profile (Eq.7). The parameters $\log \rho_0$, $\log r_h$, β , are for parameters of dark matter mass distribution. The parameters M_{thin} , M_{thick} , M_{bulge} are total mass for the thin and thick disk, and bulge components, and their units is $10^{10} M_{\odot}$. The parameters h_{thin} , h_{thick} indicate the scale-length for thin and thick disk. The contour lines in each panel and the vertical lines in the marginal histograms are shown the 16%, 50%, 84% percentiles.

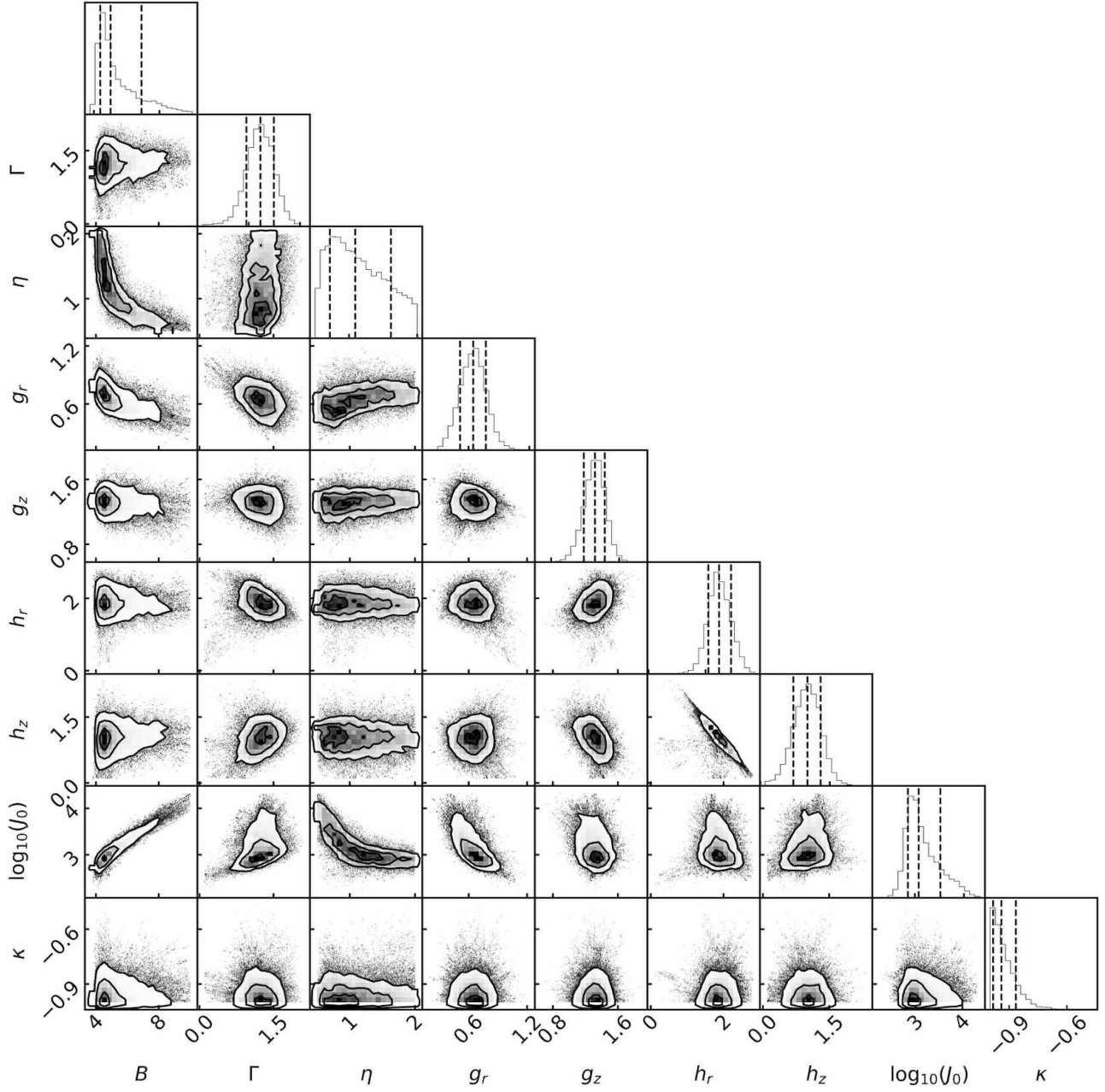


Figure A3. Posterior distribution of parameters of DF (eq. 8) of GCs with model using the Einasto's DM density profile (Eq.7). The parameters B and Γ related to the outer and inner slopes of DF, while η determine the steepness of transition. The dimensionless parameters g_r, g_z, h_r, h_z control the density shape and the velocity ellipsoid in the outer and inner region. The inner and outer regions are separated with actions J_0 . κ controls the rotation. The contour lines in each panel and the vertical lines in the marginal histograms show the 16%, 50%, 84% percentiles.

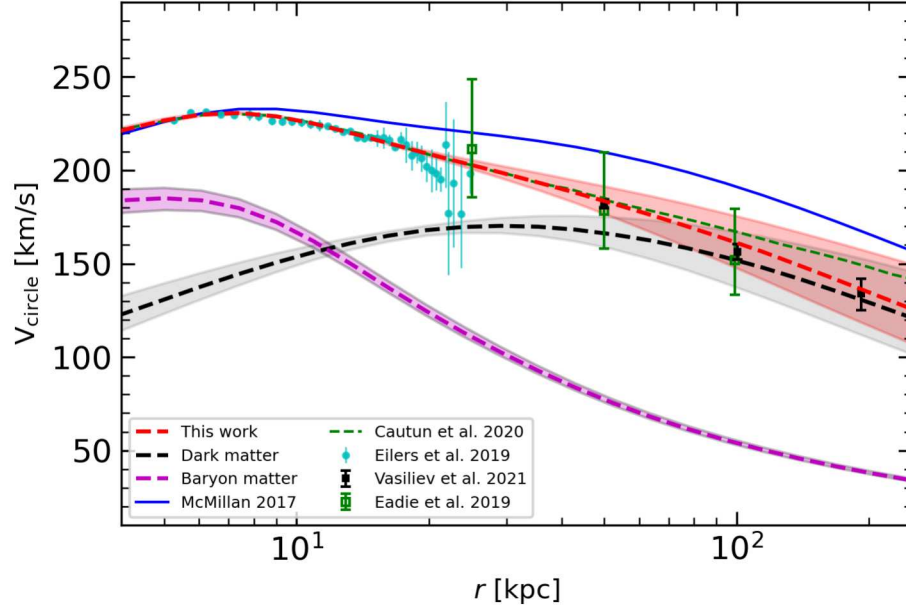


Figure B1. Comparing rotation curves derived from posterior distribution of our models with literature with GCs data from Vasiliev & Baumgardt (2021). Zhao's dark matter profile are used. The shaded region indicate the 68 percentile.